Using SIMS to decode noisy stratigraphic δ^{13}C variations in Ediacaran carbonates

Shuhai Xiao [a,*], Huan Cui [b,c,d,e], Junyao Kang [a], Kathleen A. McFadden [f], Alan J. Kaufman [g], Kouki Kitajima [d,e], John H. Fournelle [e], Maxwel Schwid [a], Morrison Nolan [a], Jean-Marc Baele [h], John W. Valley [d,e]

[a] Department of Geosciences, Virginia Tech, Blacksburg, VA 24061, U.S.A.

[b] Research Group of Analytical, Environmental and Geo- Chemistry, Division of Earth System Science, Vrije Universiteit Brussel, Brussels, Belgium

[c] ET-HOME (Evolution and Tracers of the Habitability of Mars and Earth) Astrobiology Research Consortium, Belgium

[d] NASA Astrobiology Institute, University of Wisconsin, Madison, Wisconsin 53706, U.S.A.

[e] Department of Geoscience, University of Wisconsin, Madison, Wisconsin 53706, U.S.A.

[f] ConocoPhillips, Houston, Texas 77079, U.S.A.

[g] Department of Geology, University of Maryland, College Park, MD 20742, U.S.A.

[h] Department of Geology, Faculty of Engineering, University of Mons, Mons, Belgium

[*] Corresponding author. Email address: xiao@vt.edu

Final Publication:
Xiao S, Cui H, Kang J, McFadden K, Kaufman A, Kitajima K, Fournelle J, Schwid M, Nolan M, Baele J-M, Valley JW (2020) Using SIMS to decode noisy stratigraphic δ^{13}C variations in Ediacaran carbonates. Precamb. Res. https://doi.org/10.1016/j.precamres.2020.105686

ABSTRACT

Carbonate carbon isotope ($\delta^{13}C_{carb}$) chemostratigraphy is a valuable tool in Precambrian stratigraphic correlation. The effectiveness of this tool rests on the assumption that $\delta^{13}C_{carb}$ data record global seawater signals. However, in some cases $\delta^{13}C_{carb}$ data may exhibit rapid and noisy stratigraphic variations that appear to have been influenced by authigenic or diagenetic carbonate minerals. To assess the contribution of non-primary minerals towards bulk carbonate carbon isotope values, we acquired SIMS (secondary ion mass spectrometry) $\delta^{13}C_{carb}$ data, electron microscopic data, and CL (cathodoluminescence) microscopic data from two Ediacaran successions—the lower Member II of the Doushantuo Formation in South China and the Mooifontein Member in southern Namibia. The Doushantuo samples came from a stratigraphic interval with noisy meter-scale $\delta^{13}C_{carb}$ variations up to 10‰, whereas the Mooifontein Member is characterized by consistent $\delta^{13}C_{carb}$ values with limited meter-scale variations less than ~4‰. Our data show that the meter-scale stratigraphic variations in $\delta^{13}C_{carb}$ are also mirrored in the SIMS data at µm-mm scales in both Doushantuo and Mooifontein samples. In the Doushantuo samples, SIMS $\delta^{13}C_{carb}$ values of authigenic calcite vary by up to 10‰ over µm-mm scales and can be higher or lower than those of co-existing dolomite matrix, which also appears to be affected by authigenic carbonate on the basis of petrographic observation. Bulk-sample $\delta^{13}C_{carb}$ values measured on powders microdrilled from the same SIMS specimens are within the SIMS $\delta^{13}C_{carb}$ ranges. Thus, we infer that bulk-sample $\delta^{13}C_{carb}$ values of Doushantuo samples represent mixtures of different carbonate components. The Doushantuo and Mooifontein SIMS $\delta^{13}C_{carb}$ data validate the traditional method of using chemostratigraphic consistency to evaluate authigenic/diagenetic alteration, but also caution against the conventional practice of taking the maximum values to approximate primary chemostratigraphic trends.

Keywords: SIMS, Stable carbon isotopes, Ediacaran, Chemostratigraphy, South China, Namibia

1. Introduction

Carbonate carbon isotopes ($\delta^{13}C_{carb}$) have been applied widely in paleoclimatology, paleoceanography, and chemostratigraphic correlation. This is particularly true in the study of Precambrian stratigraphic correlation (Kaufman and Knoll, 1995), because few Precambrian fossils can be considered as robust index fossils for biostratigraphic correlation. In the past four decades, available Precambrian $\delta^{13}C_{carb}$ data have grown enormously and are often the basis of Ediacaran stratigraphic correlation and subdivision (Xiao et al., 2016). These data also revealed two unusual and enigmatic features of Ediacaran $\delta^{13}C_{carb}$ chemostratigraphy. First, exceptionally large $\delta^{13}C_{carb}$ excursions, such as the Shuram negative excursion reaching –10‰ VPDB (Grotzinger et al., 2011) and the Hüttenberg positive excursion reaching +10‰ VPDB (Cui et al., 2018), have been reported from Ediacaran carbonate successions. These large excursions are difficult to explain using simple steady-state models, which limit $\delta^{13}C_{carb}$ variations between ca. –5‰ (when carbon burial is 100% carbonate) and ca. 20‰ (when carbon burial is 100% organic carbon). As a result, various non-steady-state models have been proposed to explain these exceptionally high-magnitude excursions (Rothman et al., 2003; Shields et al., 2019). Second, irregular point-to-point variations in $\delta^{13}C_{carb}$, sometimes with values between –40‰ and 6‰ at decimeter–meter scales, are observed in some Ediacaran successions such as the lower Doushantuo Formation (Jiang et al., 2003; McFadden et al., 2008; Wang et al., 2008; Zhou et al., 2016). These variations are also difficult to explain using traditional carbon cycle models, and localized anaerobic oxidation of methane during early or late diagenesis has been invoked as a major driver of such irregular and noisy stratigraphic variations in $\delta^{13}C_{carb}$ values (Jiang et al., 2003; Wang et al., 2008; Zhou et al., 2016; Cui et al., 2017; Wang et al., 2017; Cui et al., 2019). These interpretations echo hypotheses stating that extremely anomalous $\delta^{13}C_{carb}$ values and noisy stratigraphic variations may be related to the precipitation of authigenic carbonate minerals (Schrag et al., 2013; Sun and Turchyn, 2014), meteoric and burial diagenesis (Knauth and Kennedy, 2009; Derry, 2010), mixing of sediments derived from different environments with different isotopic signatures (Swart, 2008), and rock-fluid interactions (Higgins et al., 2018; Hoffman and Lamothe, 2019). Such secondary or authigenic/diagenetic processes challenge the basic premise of $\delta^{13}C_{carb}$ chemostratigraphy, which assumes that bulk $\delta^{13}C_{carb}$ records primary dissolved inorganic carbon isotopic signatures of the global ocean. Addressing this challenge requires in-situ, micrometer-scale $\delta^{13}C$ data coupled with diligent petrographic analysis in order to tease apart $\delta^{13}C$ signatures between sedimentary and diagenetic components. Secondary ion mass spectrometry (SIMS) offers a powerful tool to address this issue because it can achieve the necessary spatial resolution and it has recently been calibrated and tested for $\delta^{13}C$ and $\delta^{18}O$ analysis of carbonate minerals (Valley and Kita, 2009; Śliwiński et al., 2016b; Denny et al., 2020; Turnier et al., 2020).

In this study, we used SIMS to analyze $\delta^{13}C_{carb}$ of four Ediacaran samples, three from the lower Doushantuo Formation in South China and one from the Mooifontein Member in southern Namibia. The Doushantuo samples were chosen because they came from a stratigraphic interval with noisy $\delta^{13}C_{carb}$ variations and they contain authigenic carbonate components that can be independently identified via petrography and cathodoluminescence (CL) microscopy. The Mooifontein sample, on the other hand, came from a stratigraphic interval with more consistent $\delta^{13}C_{carb}$ values and a limited range of variations, thus offering a comparison with the Doushantuo samples. The main goals of this study are to test (1) whether the meter-scale stratigraphic variations in $\delta^{13}C_{carb}$, which are up to 10‰ in the lower Doushantuo Formation and ~4‰ in the Mooifontein Member, are also captured in the SIMS data at µm-mm scale; (2) whether $\delta^{13}C_{carb}$ values of authigenic/diagenetic carbonate are distinct from, higher than, or lower than bulk-sample $\delta^{13}C_{carb}$ values measured from microdrilled powders; and (3) whether $\delta^{13}C_{carb}$ analysis of microdrilled powders represent a mixture of sedimentary and authigenic signatures. By answering these questions, we hope to demonstrate that SIMS is a useful tool to evaluate the influence of authigenic/diagenetic carbonate minerals on $\delta^{13}C_{carb}$ values of microdrilled powders.

2. Geological and stratigraphic background

The three Doushantuo samples were collected from lower Member II of the Doushantuo Formation at the well-studied Jiulongwan section in the Yangtze Gorges area of South China. At Jiulongwan, the Doushantuo Formation is about 154 m thick and can be divided into four members (Fig. 1; see published and new $\delta^{13}C_{carb}$ data in Supplementary Data 1). Member I is ca. 4 m thick and represents the cap dolostone directly overlying terminal Cryogenian glaciogenic diamictite of the Nantuo Formation. It is characterized by negative $\delta^{13}C_{carb}$ values around –3.5‰, representing the negative excursion labeled "EN1" in Fig. 1. However, localized occurrences of extremely negative $\delta^{13}C_{carb}$ values as low as –48‰ have been reported from void-filling calcite cement (Jiang et al., 2003; Wang et al., 2008; Zhou et al., 2010; Bristow et al., 2011; Zhou et al., 2016; Wang et al., 2017; Cui et al., 2019). The origin of these extremely negative $\delta^{13}C_{carb}$ signatures is a matter of debate, with interpretations ranging from early diagenetic or authigenic calcite cement related to methane gas hydrate release that led to the termination of the terminal Ediacaran snowball Earth glaciation (Jiang et al., 2003; Wang et al., 2008), to late diagenetic calcite cement related to the oxidation of thermogenic methane (Bristow et al., 2011; Cui et al., 2019). Member II is ca. 71 m thick (meterage ca. 4–75 m in Fig. 1) and consists of argillaceous dolostone interbedded with mudstone. Microdrilled powders (hereafter bulk samples) generally have positive $\delta^{13}C_{carb}$ values, representing the positive excursion labeled "EP1" in Fig. 1, although the lower part of Member II is characterized by noisy stratigraphic variations between –5‰ and 7‰. Fossiliferous chert nodules, as well as calcite nodules, are present in this member and they preserve a diverse assemblage of acanthomorphic acritarchs (Zhang et al., 1998; Xiao, 2004; McFadden et al., 2009; Liu and Moczydłowska, 2019). These chert nodules typically consist of a silica core surrounded by a pyrite and calcite rim. Petrographic and SIMS $\delta^{34}S_{pyrite}$ data indicate that these chert nodules were lithified during early diagenesis (Xiao et al., 2010). Member III is ca. 65 m thick (meterage ca. 75–141 in Fig. 1), with thick-bedded dolostone in the lower interval and ribbon rocks (i.e., thin-bedded limestone with thin argillaceous dolostone intercalations) in the upper interval. Acanthomorphic acritarchs and other microfossils have been reported from chert nodules and bands in Member III (Zhang et al., 1998; Liu et al., 2014; Liu and Moczydłowska, 2019). Bulk-sample $\delta^{13}C_{carb}$ values register a negative excursion (labeled "EN2" in Fig. 1) at the Member II–III transition, followed by a positive excursion ("EP2" in Fig. 1) in the lower Member III and then a pronounced negative excursion (–10‰; "EN3" in Fig. 1) in the upper portion of Member III. The negative excursion EN3 continues into Member IV (meterage 141–154.1 m in Fig. 1), where negative $\delta^{13}C_{carb}$ values are measured from dolomite concretions hosted in black shales. The negative excursion EN3 is thought to be equivalent to the Shuram negative excursion recorded in Oman (Grotzinger et al., 2011; Zhou et al., 2017a).

The three Doushantuo samples analyzed in this study—JLW15.1, JLW23.5, JLW35.2—were collected from lower Member II, at stratigraphic horizons 15.1 m, 23.5 m, and 35.2 m, respectively, above the base of the Doushantuo Formation (Fig. 1). Radiometric dates from ash beds in the Doushantuo Formation in the Yangtze Gorges area constrain the depositional age of these three samples between 632.5 ± 0.5 Ma and 551.1 ± 0.7 Ma (Condon et al., 2005). We note that 551.1 ± 0.7 Ma age came from an ash bed at the uppermost Miaohe Member at a nearby section in the Yangtze Gorges area and the correlation between the Miaohe Member and Member IV has yet to be confirmed (An et al., 2015; Xiao et al., 2017; Zhou et al., 2017a). Regardless of whether the Miaohe Member is partially equivalent to or younger than Member IV, the 551.1 ± 0.7 Ma age remains a minimum constraint on the depositional age of the three analyzed samples. Via lithostratigraphic correlation, additional radiometric dates from the Doushantuo Formation at the Jiuqunao section in the Yangtze Gorges area (Condon et al., 2005) and in the Zhangcunping area to the north of the Yangtze Gorges (Liu et al., 2009; Zhou et al., 2017b) indicate that JLW15.1 and JLW23.5 are likely between 632.5 ± 0.5 Ma and 614.0 ± 7.6 Ma, and JLW35.2 between 614.0 ± 7.6 Ma and 609 ± 5 Ma (Fig. 1). These age constraints are consistent with an astronomical time scale for the lower Doushantuo Formation, which places the first 22 m of the Doushantuo Formation between 636.8 ± 0.7 Ma and 625.6 ± 0.7 Ma (Sui et al., 2018).

The Mooifontein sample, 2016AarFarm, was collected from the Mooifontein Member, Zaris Formation, Kuibis Subgroup, Nama Group at an outcrop (26.75036°S, 16.49832°E) about 4.5 km southeast of Farm Aar in the Witpus sub-basin of southern Namibia (Vickers-Rich et al., 2016). The Mooifontein Member near Farm Aar is more than 40 m thick (Fig. 2; see published and new $\delta^{13}C_{carb}$ data in Supplementary Data 2), with its upper boundary truncated by modern erosion. It was deposited in oxic to manganous suboxic environments on a carbonate ramp in the terminal Ediacaran Period (Saylor et al., 1998; Wood et al., 2015; Tostevin et al., 2016). It consists of thin- to medium-bedded limestone and contains abundant calcareous tubular fossils of

Cloudina riemkeae (Fig. 3d–f) (Grant, 1990). Bulk-sample $\delta^{13}C_{carb}$ values of the Mooifontein Member are mostly in the range of 0–4‰ (Saylor et al., 1998; Wood et al., 2015; Vickers-Rich et al., 2016), much narrower than the ~10‰ range documented in the lower Doushantuo Formation at Jiulongwan. The depositional age of the Mooifontein Member is constrained by a radiometric date of 548.8 ± 1 Ma (Grotzinger et al., 1995), subsequently recalculated as 547.32 ± 0.31 Ma (Schmitz, 2012), from the Zaris Formation in the Zaris sub-basin of southern Namibia.

3. Methods

3.1. Sample preparation

Three Doushantuo samples (JLW15.1, JLW23.5, JLW35.2) that contain chert nodules and one Mooifontein sample (2016AarFarm) that contains internal molds of *Cloudina riemkeae* were chosen for this study. The hand samples were trimmed to remove weathered surfaces and cut in half to prepare mirrored thin and thick sections for petrographic and SIMS analyses, respectively. Thin sections were examined on a standard transmitted light petrographic microscope. For SIMS sample preparation, a one-inch diameter billet was extracted from the thick section. Five one-millimeter drill holes were made on the one-inch round thick section, and anthracite, quartz, dolomite, calcite, and pyrite standards were placed in these drill holes and secured with epoxy. Only the calcite standard UWC-3 and the dolomite standard UW6220 were used in this study, and the other standards will be used in future SIM analyses of organic C, silica O, and pyrite S isotopic compositions. The round thick section with the standards was then polished to microprobe grade for analyses using reflected light microscopy, SEM (scanning electron microscopy), SIMS, EPMA (electron probe microanalysis), and cathodoluminescence (CL) microscopy.

3.2. Pre-SIMS light microscopic and SEM imaging

Reflected light microscopic and SEM images of polished thick sections were produced to guide the selection of SIMS analytical spots. SEM (scanning electron microscopy) was performed in the Ray and Mary Wilcox Scanning Electron Microscopy Laboratory, Department of Geoscience, University of Wisconsin–Madison. BSE (back scattered electron) SEM images were acquired with a Hitachi S3400 VP SEM with EDS (energy dispersive spectrometry) using a Thermo Fisher thin window detector. SEM images were acquired using an accelerating voltage of 15 keV. Areas (domains) selected for SIMS analysis were imaged at various magnifications and these images were used to help navigate during SIMS sessions.

3.3. SIMS

SIMS analyses were conducted on a CAMECA IMS 1280 at the WiscSIMS (Wisconsin Secondary Ion Mass Spectrometry) Lab, Department of Geoscience, University of Wisconsin–Madison. The analyses include three SIMS sessions. During the sessions (Mar. 15–17, 2017), carbon two–isotopes (^{12}C, ^{13}C) were measured with a 7-µm-diameter beam size. Measurements of $\delta^{13}C$ were made using one Faraday cup and two electron multiplier detectors measuring $^{12}C^-$, $^{13}C^-$, and $^{13}C^1H^-$, respectively. The UWC-3 calcite standard and the UW6220 dolomite standard were used to calibrate analyses of carbon isotopes (Valley and Kita, 2009; Śliwiński et al., 2016b). Carbon isotope ratios are reported in standard per mil (‰) notation relative to VPDB, calculated as $\delta^{13}C_{unknown} = [(^{13}C/^{12}C)_{unknown} / (^{13}C/^{12}C)_{VPDB} - 1] \times 1000$. Measured ratios of $^{13}C/^{12}C$ were calculated as "raw" δ–values ($\delta^{13}C_{raw}$) before converting to the VPDB scale (see below) based on eight analyses of a running standard (UWC-3) that bracket each group of 10–15 sample analyses. The entire dataset can be found in Supplementary Data 3–4.

Measurements of $^{13}C/^{12}C$ were made using a $^{133}Cs^{+}$ primary ion beam with an intensity of ~600 pA. The secondary ion intensity of ^{12}C was ~7×10^{6} cps. ^{13}CH was analyzed to evaluate the effect of hydrogen, which might be in the form of organic matter or water, on the SIMS results. An electron flood gun in combination with a gold coating (~40 nm) was used for charge compensation. The total analytical time per spot was about 4 minutes including pre-sputtering (20 s), automatic centering of the secondary ion beam in the field aperture (60 s), and analysis (160 s). Applied high-voltage on EM for ^{13}C was automatically adjusted after every analysis. The baseline noise level of the Faraday cup was measured at the beginning of each analysis day.

The raw isotope ratios obtained by SIMS are biased by an instrumental mass fractionation (IMF or bias) that can vary in magnitude depending on instrumental conditions, mineralogy, and sample composition (Śliwiński et al., 2016b). To address the effect of Fe/Mg on IMF, a suite of standards along the dolomite-ankerite series were analyzed at the beginning of the session and used to generate a calibration curve relative to the running standard UW6220 (Valley and Kita, 2009; Śliwiński et al., 2016b; Śliwiński et al., 2016a; Denny et al., 2020). After SIMS analysis, this calibration curve was used to determine the composition-specific IMF based on the Fe concentration (Fe# = molar Fe/[Fe+Mg]; determined using an electron microprobe, see EPMA procedures below) of each SIMS pit. We also applied matrix correction regarding Mg, Fe and Mn in calcite. Details can be found in Turnier et al. (2020). The spot-to-spot precision of $\delta^{13}C$ values based on all bracketing analyses on standard UWC-3 is ±0.6‰ (2SD; see Supplementary Data 3).

3.4. Post-SIMS SEM, EPMA, and CL microscopic analyses

After SIMS analysis, the gold coating was removed before further SEM, EPMA, and CL microscopic analyses. SEM imaging was performed in the Ray and Mary Wilcox Scanning Electron Microscopy Laboratory, Department of Geoscience, University of Wisconsin–Madison. BSE images of carbon–coated samples were acquired with a Hitachi S3400 VP SEM with EDS using a Thermo Fisher thin window detector. Each SIMS pit was examined by SEM for possible irregularities. SEM images were acquired using an accelerating voltage of 15 keV or 20 keV at a working distance of 10 mm. All the SIMS pits were imaged by SEM and are shown with corresponding δ^{13}C values in Supplementary Data 4.

Electron probe microanalysis (EPMA) was conducted in the Eugene Cameron Electron Microbeam Lab, Department of Geoscience, University of Wisconsin–Madison. EPMA was performed with the CAMECA SXFive field emission electron probe, operated at 20 kV and 50 nA, and either a focused beam or a 3–4 µm defocused beam, using wavelength dispersive crystal spectrometers (Supplementary Data 3). Counting times were 10 seconds on peak and 10 seconds on background, for all elements except those noted in the following listing. Al Kα (20 sec) and Si Kα (20 sec) were acquired on a large TAP crystal; As Kα (20 sec) and Se Kα (20 sec) on LIF; S Kα and Ca Kα (27 sec) on large PET; Fe Kα, Mn Kα and Co Kα on LIF; and Ni Kα, Cu Kα and Zn Kα on large LIF. Standards used were Balmat pyrite (Fe, S), NBS glass K412 (Si, Al, Ca), arsenopyrite (As), and freshly polished metals for the balance. PHA modes used were integral, except for Al and Si which were differential mode. Software used was Probe for EPMA (Donovan et al., 2018). Off peak backgrounds were acquired, and matrix correction was conducted using the Armstrong/Love Scott algorithm (Armstrong, 1988). EPMA data are presented in Supplementary Data 3.

Cathodoluminescence (CL) microscopy was carried out at University of Mons, Belgium. Cathodoluminescence excitation was achieved with a cold cathode CITL CL system (Cambridge Image Technology - model Mk5, UK). The unit was operated at 15 kV and 500 µA acceleration voltage and beam current, respectively. With these settings, the unfocused beam had a current density of about 8 µA/mm^2. Cathodoluminescence microscopic images were captured with a Peltier-cooled digital color camera (Lumenera model Infinity 4, Canada), set from 0.1 s to a few seconds exposure time depending on CL intensity and microscope magnification. Multiple frame averaging was used to reduce noise. Color calibration of the camera (white balance) was performed using the blue-filtered, tungsten-halogen light source of the microscope, which may result in CL colors that are slightly different from other equipment (especially around the yellow band, which is narrow) but ensures more or less standardized observation conditions.

4. Results

4.1. Petrographic observations

Petrographic observations were made using petrographic microscopy (Fig. 3), backscattered SEM (Figs, 4, 6, 8, 10, and 12), secondary electron SEM (Supplementary Data 4), and CL microscopy (Figs. 5, 7, 9, 11, and 13), to independently identify different carbonate phases, including authigenic or early diagenetic carbonate; the term authigenesis is used here as a synonym of early diagenesis or pre-compaction diagenesis. Key petrographic observations support that the chert nodules in JLW15.1, JLW23.5, and JLW35.2 were silicified during early diagenesis. These observations include: (1) sedimentary microlaminae in the dolostone matrix warp around the chert nodules (Fig. 3b–c), indicating that the chert nodules were lithified before compaction; (2) sedimentary microlaminae are also preserved within the chert nodules, but they are more widely spaced than those outside the chert nodules (Fig. 3b–c), consistent with the pre-compaction lithification of the chert nodules; and (3) some chert nodules contain exceptionally preserved microfossils (Xiao et al., 2004; Xiao et al., 2010), often in three dimensions, again suggesting silicification occurred prior to compaction.

The chert nodules typically consist of a silica core surrounded by a pyrite rim and a calcite rim (Figs. 3a–c, 4a, 6a, 8a). The relative portions of the silica core, pyrite rim, and calcite rim can vary. For example, some chert nodules in JLW35.2 are dominated by a proportionally large calcite rim, with a reduced silica core and sometimes lacking a well-defined pyrite rim. In any case, most chert nodules are sharply defined by a pyrite/calcite rim that is petrographically distinct from the dolomite matrix (Fig. 3a–c). Thus, like the silica core, the pyrite and calcite rims are also likely early diagenetic in origin, although the calcite rim may post-date the silica core (Xiao et al., 2010). McFadden et al. (2008) and Xiao et al. (2010) analyzed two of the three Doushantuo samples for bulk-sample $\delta^{34}S_{pyrite}$ using the chromium reduction method and $\delta^{34}S_{pyrite}$ of individual pyrite crystals in the matrix and in the pyrite rims using SIMS: JLW23.5 (bulk-sample matrix pyrite $\delta^{34}S$ = 16.4‰ CDT; SIMS rim pyrite $\delta^{34}S$ = 15.2–20.3‰ CDT, average ± 1 s.d. = 18.1 ± 1.2‰ CDT, n =28; SIMS matrix pyrite $\delta^{34}S$ = 24.4–39.8‰ CDT, average ± 1 s.d. = 30.6 ± 4.7‰ CDT, n = 8) and JLW15.1 (bulk-sample matrix pyrite $\delta^{34}S$ = 7.9‰ CDT; SIMS rim pyrite $\delta^{34}S$ = 19.2–27.3‰ CDT, average ± 1 s.d. = 24.6 ± 1.6‰ CDT, n =34). The positive and highly variable $\delta^{34}S_{pyrite}$ values indicate continuous sulfate reduction and pyrite precipitation in pore waters with limited supply of seawater sulfate, suggesting that localized microbial processes (e.g., microbial sulfate reduction) may have played a critical role in the formation of the pyrite rim during early diagenesis (Xiao et al., 2010).

In addition to the calcite rim surrounding chert nodules, there are other carbonate phases in the Doushantuo samples that can be targeted for SIMS $\delta^{13}C_{carb}$ analysis. Some Doushantuo nodules have a relatively small silica core surrounded by a thick calcite rim (e.g., Domain 3 in Fig. 8a; Fig. 10a) and thus would be more appropriately called calcite nodules, which can easily be analyzed using SIMS. In addition, there are small patches of calcite cements in the nodule interior and within the dolomite matrix. These patches are sometimes elongate in shape and conform to bedding (e.g., Fig. 8b upper right; 8d lower right; 8e). They do not seem to be post-compaction dissolution vugs that were subsequently filled with cements. Instead, they are interpreted as authigenic calcite cement that formed prior to sediment compaction, because porosity needed for the precipitation of such cement patches would have been greatly reduced after compaction. In a sense, these patches of cement can be regarded as smaller versions of calcite nodules shown in Figure 10a. Thus, there are multiple phases of calcite cements, possibly representing one or more generations of cementation, that can be targeted for SIMS analysis. Finally, the dolomite matrix can also be targeted for SIMS analysis, as long as the effect of diffuse organic matter in the matrix is carefully evaluated by monitoring the ^{13}CH peak.

The Mooifontein sample (16AarFarm) consists of homogeneous and coarsely recrystallized limestone. The tubular fossil *Cloudina riemkeae* is abundant. Most *Cloudina* specimens are preserved as internal molds, with the test lost and the interior of the tube filled with calcite (Fig. 3d). Bulk-sample $\delta^{13}C_{carb}$ values of the Mooifontein Member are consistently in the range of 1–4‰, as measured in multiple sections in the Witpus sub-basin (Saylor et al., 1998; Wood et al., 2015; Vickers-Rich et al., 2016). Because of the homogeneous nature of this sample, SIMS analysis is targeted on the calcite crystals in a mold of *Cloudina* (i.e., within *Cloudina* tube; Fig. 12a) and in the matrix (i.e., outside *Cloudina* tube; Fig. 12b).

4.2. SIMS $\delta^{13}C_{carb}$, bulk-sample $\delta^{13}C_{carb}$, and *EPMA data*

SIMS $\delta^{13}C_{carb}$ and EPMA elemental measurements are provided in Supplementary Data 3. All SIMS $\delta^{13}C_{carb}$ data are mapped on post-SIMS secondary electron SEM images showing SIMS pits (Supplementary Data 4). SIMS $\delta^{13}C_{carb}$ values are also mapped on back-scattered electron SEM images and CL images of analytical domains (Figs. 4–13). SIMS $\delta^{13}C_{carb}$ are summarized in Fig. 14. The relationships between SIMS $\delta^{13}C_{carb}$, carbonate components, and elemental concentrations are shown in Fig. 15.

In the three Doushantuo samples, SIMS $\delta^{13}C_{carb}$ shows large spatial variations at µm-mm scales within the calcite rim, generally over 5‰ and in some cases greater than 10‰ (e.g., Figs. 6d, 10b). In contrast, the Mooifontein sample shows much lower-magnitude spatial variability, with an overall range of 4.4‰ but typically <1‰ at the µm-scale. The difference in variability between the Doushantuo and Mooifontein samples is illustrated in Fig. 14, with the former showing much greater ranges and standard deviation values than the latter.

Spatial variations in SIMS $\delta^{13}C_{carb}$ at µm-mm scales (histograms and box-and-whisker plots in Fig. 14) roughly match the stratigraphic $\delta^{13}C_{carb}$ variations at meter scales measured by acid dissolution and gas source mass spectrometry (red double-arrowed lines in Fig. 14). For the Doushantuo samples, the stratigraphic variations shown in Fig. 14 represent the range of bulk-sample $\delta^{13}C_{carb}$ values in strata one meter above and below the SIMS sample, which approximately represent variations over ~1 Myr according to an astronomically tuned time scale for the lower Doushantuo Formation at the Jiulongwan section (Sui et al., 2018). For the Mooifontein samples, the stratigraphic variation shown in Fig. 14 represents the range of bulk-sample $\delta^{13}C_{carb}$ values in the 40 m strata of the Mooifontein Member (Wood et al., 2015; Vickers-Rich et al., 2016).

Bulk-sample $\delta^{13}C_{carb}$ values measured on powders drilled from the matrix of the same samples used for SIMS analysis are denoted by green arrows in Fig. 14. In all cases, the bulk-sample $\delta^{13}C_{carb}$ values are within the ranges of SIMS $\delta^{13}C_{carb}$ values and for the Doushantuo samples, the bulk-sample measurements are in the central 50% percentile of SIMS measurements (Figs. 14, 15a).

In Fig. 15b, SIMS $\delta^{13}C_{carb}$ data are categorized according to different carbonate phases. Not only do the various authigenic calcite components (e.g., calcite rims, calcite nodules, and calcite cements) show spatial variability in $\delta^{13}C$, the dolomite matrix is also characterized by variable $\delta^{13}C$ data (symbols filled in gray in Fig. 15b–c; data only available for JLW23.5). The variation in matrix $\delta^{13}C$ is probably caused by the occurrence of authigenic carbonate in the matrix, as evidence from the CL images revealing carbonate minerals with multiple CL colors (e.g., Figs. 9e, 11c, 11g). It is important to note that individual $\delta^{13}C$ measurements of authigenic calcite can be either higher or lower than those of dolomite matrix.

When SIMS $\delta^{13}C_{carb}$ data are plotted against Mg, Mn, and Fe contents as determined by EPMA, no systematic correlations are observed (Fig. 15c–f). Thus, it is unlikely that the µm-mm scale variations in $\delta^{13}C$ are related to the calibration of SIMS data, which uses the elemental concentration of Mg, Mn, and Fe (Śliwiński et al., 2016b; Śliwiński et al., 2016a; Denny et al., 2020; Turnier et al., 2020).

5. Discussion

The noisy $\delta^{13}C$ profile in the lower Doushantuo Formation is an enigmatic feature that complicates chemostratigraphic correlation. Some authors considered such noisy variations chemostratigraphically significant and attempted to identify regionally correlatable negative $\delta^{13}C$ excursions in the lower Member II of the Doushantuo Formation (Tahata et al., 2013; Zhu et al., 2013; Gao et al., 2018). For example, the negative $\delta^{13}C$ excursion WANCE from the lower Member II has been proposed as a chemostratigraphic marker in South China (Zhu et al., 2013). However, the chemostratigraphic value of such excursions has been questioned because they occur in a stratigraphic interval with highly variable $\delta^{13}C$ values and are not regionally consistent (Zhou and Xiao, 2007; Xiao et al., 2012). The SIMS data presented here help us to understand the potential origin of these excursions and to dissect the noisy chemostratigraphic trend in the lower Member II of the Doushantuo Formation.

Given the spatial variation in SIMS $\delta^{13}C$ data at μm-mm scales, we propose that the noisy $\delta^{13}C$ profiles in the lower Member II likely represent variable mixing of different carbonate phases, including sedimentary dolomite, authigenic calcite cement, and even late diagenetic carbonate components. Because the dolomite matrix can also contain authigenic carbonate minerals (e.g., Figs. 9e, 11c, 11g) with highly variable $\delta^{13}C$ at μm-mm scales, as shown in sample JLW23.5 (Figs. 8–9), sampling via microdrilling in an attempt to avoid calcite cements and veins is unlikely to mitigate this problem. Thus, we caution against the use of noisy $\delta^{13}C$ excursions in the lower Member II for regional or global chemostratigraphic correlation.

The origin of μm-mm scale $\delta^{13}C$ variations in the lower Member II remains uncertain. However, given that this stratigraphic unit in South China is widely influenced by methanogenesis and methane oxidation (Jiang et al., 2003; Wang et al., 2008; Zhou et al., 2016), it is possible that the µm-mm scale $\delta^{13}C$ variations may be related to pore-water microbial and diagenetic processes that control methane oxidation. Together, methanogenesis and methane oxidation can result in highly variable $\delta^{13}C$ signatures in authigenic carbonate (Meister et al., 2018), depending on whether methane is oxidized in situ or escapes from sediments, and whether it is oxidized aerobically or anaerobically.

This study has several broader implications for $\delta^{13}C$ chemostratigraphy. First, integrated SIMS and petrographic analyses offer a powerful tool to individually interrogate different generations of carbonate cement (Denny et al., 2020), to evaluate the influence of authigenic/diagenetic carbonate minerals on $\delta^{13}C$ chemostratigraphy, and to dissect the origin of noisy chemostratigraphic trends. The data presented here show that chemostratigraphic variations at meter scales can be captured at the µm-mm scales, the latter reflecting the influence of authigenic/diagenetic carbonate minerals. Thus, our study verifies the traditional view that noisy chemostratigraphic trends are suggestive of diagenetic alteration, and indicates that chemostratigraphic consistency is a useful tool to evaluate diagenetic alteration. In our case study, for example, the lower Member II of the Doushantuo Formation was probably influenced by authigenic/diagenetic alteration to a greater degree than the Mooifontein Member.

Our study also casts doubt on the traditional practice of taking the maximum $\delta^{13}C$ values to approximate primary chemostratigraphic trends. As shown in the Doushantuo samples, $\delta^{13}C$ values of authigenic calcite can be greater or lower than those of the dolomitic matrix, making it difficult to infer primary chemostratigraphic trends from noisy data using either the maximum values or moving averages. In such cases, coupled SIMS and petrographic analysis is an indispensable tool to disentangle the paragenetic sequence and isotopic signals from noisy data.

6. Conclusions

By contrasting the Doushantuo and Mooifontein data, we show that meter-scale chemostratigraphic variations in $\delta^{13}C_{carb}$ (up to 10‰ in the lower Member II of the Doushantuo Formation and ~4‰ in the Mooifontein Member) are also captured in SIMS $\delta^{13}C_{carb}$ variations at µm-mm scale. In the Doushantuo samples, petrographically identified authigenic calcite—which may have been influenced by localized pore-water processes such as methanogenesis and methane oxidation—has a wider range of SIMS $\delta^{13}C_{carb}$ values and can be isotopically heavier or lighter than co-existing dolomite matrix. In both the Doushantuo and Mooifontein samples, the range of SIMS $\delta^{13}C_{carb}$ values encompasses bulk-sample $\delta^{13}C_{carb}$ values measured on microdrilled powders, suggesting that, in some cases, even micro-sampling may incorporate a quantitatively significant proportion of authigenic/diagenetic components, such as cements, which may be isotopically distinct from sedimentary signatures. With its capability to obtain accurate µm-mm scale $\delta^{13}C_{carb}$ data and when integrated with detailed petrographic and microscopic data, SIMS is a powerful technique to understand the origin of noisy chemostratigraphic patterns. The data presented here confirm that, not surprisingly, only stratigraphically consistent $\delta^{13}C_{carb}$ data are useful in chemostratigraphic correlation, and indicate that the traditional practice of taking the maximum $\delta^{13}C_{carb}$ values to approximate primary chemostratigraphic trends can be misleading.

Acknowledgements

This research was supported by NASA Exobiology and Evolutionary Biology Program (80NSSC18K1086) and NSF Sedimentary Geology and Paleobiology Program (EAR-1528553).

WiscSIMS is supported by NSF (EAR-1658823) and the University of Wisconsin at Madison. KK and JWV were supported by the US Dept. of Energy, Office of Basic Energy Sciences (Geosciences) under Award Number DE-FG02-93ER14389. HC and JWV were supported by the NASA Astrobiology Institute (NAI–14467ZB). The authors would like to thank Huifang Xu for assistance in light microscopy; Brian Hess, Noriko Kita, James Kern, Maciej Śliwiński, Mike Spicuzza for assistance in SIMS sample preparation and SIMS analysis.

An, Z., Jiang, G., Tong, J., Tian, L., Ye, Q., Song, H., Song, H., 2015. Stratigraphic position of the Ediacaran Miaohe biota and its constrains on the age of the upper Doushantuo $\delta^{13}C$ anomaly in the Yangtze Gorges area, South China. Precambrian Research 271, 243–253. https://doi.org/10.1016/j.precamres.2015.10.007.

Armstrong, J.T., 1988. Quantitative analysis of silicate and oxide minerals: comparison of Monte Carlo, ZAF and phi-rho-z procedures. Microbeam Analysis 23, 239–246.

Bristow, T.F., Bonifacie, M., Derkowski, A., Eiler, J.M., Grotzinger, J.P., 2011. A hydrothermal origin for isotopically anomalous cap dolostone cements from south China. Nature 474, 68-71.

Condon, D., Zhu, M., Bowring, S., Wang, W., Yang, A., Jin, Y., 2005. U-Pb ages from the Neoproterozoic Doushantuo Formation, China. Science 308, 95-98.

Cui, H., Kaufman, A.J., Xiao, S., Zhou, C., Liu, X., 2017. Was the Ediacaran Shuram Excursion a globally synchronized early diagenetic event? Insights from methane-derived authigenic carbonates in the uppermost Doushantuo Formation, South China. Chemical Geology 450, 59-80. https://doi.org/10.1016/j.chemgeo.2016.12.010.

Cui, H., Kaufman, A.J., Peng, Y., Liu, X.-M., Plummer, R.E., Lee, E.I., 2018. The Neoproterozoic Hüttenberg $\delta^{13}C$ anomaly: Genesis and global implications. Precambrian Research 313, 242-262. https://doi.org/10.1016/j.precamres.2018.05.024.

Cui, H., Orland, I.J., Denny, A., Kitajima, K., Fournelle, J.H., Baele, J.-M., De Winter, N.J., Goderis, S., Claeys, P., Valley, J.W., 2019. Ice or fire? Constraining the origin of isotopically anomalous cap carbonate cements by SIMS. Geological Society of America Abstracts with Programs 51(5), 10.1130/abs/2019AM-332456.

Denny, A.C., Orland, I.J., Valley, J.W., 2020. Regionally correlated oxygen and carbon isotope zonation in diagenetic carbonates of the Bakken Formation. Chemical Geology 531, 119327. https://doi.org/10.1016/j.chemgeo.2019.119327.

Derry, L.A., 2010. A burial diagenesis origin for the Ediacaran Shuram-Wonoka carbon isotope anomaly. Earth and Planetary Science Letters 294, 152-162. https://doi.org/10.1016/j.epsl.2010.03.022.

Donovan, J.J., Kremser, D., Fournelle, J., Goemann, K., 2018. Probe for Windows User's Guide and Reference, Enterprise Edition. Probe Software, Inc., Eugene, OR.

Gao, Y., Zhang, X., Zhang, G., Chen, K., Shen, Y., 2018. Ediacaran negative C-isotopic excursions associated with phosphogenic events: Evidence from South China. Precambrian Research 307, 218-228. https://doi.org/10.1016/j.precamres.2018.01.014.

Grant, S.W.F., 1990. Shell structure and distribution of *Cloudina*, a potential index fossil for the terminal Proterozoic. American Journal of Science 290-A, 261-294.

Grotzinger, J.P., Fike, D.A., Fischer, W.W., 2011. Enigmatic origin of the largest-known carbon isotope excursion in Earth's history. Nature Geoscience 4, 285-292. https://doi.org/10.1038/NGEO1138.

Grotzinger, J.P., Bowring, S.A., Saylor, B.Z., Kaufman, A.J., 1995. Biostratigraphic and geochronologic constraints on early animal evolution. Science 270, 598-604.

Hall, M., Kaufman, A.J., Vickers-Rich, P., Ivantsov, A.Y., Trusler, P., Linnemann, U., Hofmann, M., Elliott, D., Cui, H., Fedonkin, M.A., Hoffmann, K.-H., Wilson, S., Schneider, G., Smith, J., 2013. Stratigraphy, palaentology and geochemistry of the late Neoproterozoic Aar Member, southwest Namibia: reflecting environmental controls on Ediacara fossil preservation during the terminal Proterozoic in African Gondwana. Precambrian Research 238, 214-232. https://doi.org/10.1016/j.precamres.2013.09.009.

Higgins, J.A., Blättler, C.L., Lundstrom, E.A., Santiago-Ramos, D.P., Akhtar, A.A., Ahma, A.-S.C., Bialik, O., Holmden, C., Bradbury, H., Murray, S.T., Swart, P.K., 2018. Mineralogy, early marine diagenesis, and the chemistry of shallow-water carbonate sediments. Geochimica et Cosmochimica Acta 220, 512-534. https://doi.org/10.1016/j.gca.2017.09.046.

Hoffman, P.F., Lamothe, K.G., 2019. Seawater-buffered diagenesis, destruction of carbon isotope excursions, and the composition of DIC in Neoproterozoic oceans. Proceedings of the National Academy of Sciences of the United States of America 116, 18874-18879. https://doi.org/10.1073/pnas.1909570116.

Jiang, G., Kennedy, M.J., Christie-Blick, N., 2003. Stable isotopic evidence for methane seeps in Neoproterozoic postglacial cap carbonates. Nature 426, 822-826.

Jiang, G., Kaufman, A.J., Christie-Blick, N., Zhang, S., Wu, H., 2007. Carbon isotope variability across the Ediacaran Yangtze platform in South China: Implications for a large surface-to-deep ocean $\delta^{13}C$ gradient. Earth and Planetary Science Letters 261, 303-320.

Kaufman, A.J., Knoll, A.H., 1995. Neoproterozoic variations in the C-isotope composition of sea water: Stratigraphic and biogeochemical implications. Precambrian Research 73, 27-49.

Knauth, L.P., Kennedy, M.J., 2009. The late Precambrian greening of the Earth. Nature 460, 728-732.

Liu, P., Moczydłowska, M., 2019. Ediacaran microfossils from the Doushantuo Formation chert nodules in the Yangtze Gorges area, South China, and new biozones. Fossils and Strata 65, 1-172. https://doi.org/10.1002/9781119564195.

Liu, P., Yin, C., Gao, L., Tang, F., Chen, S., 2009. New material of microfossils from the Ediacaran Doushantuo Formation in the Zhangcunping area, Yichang, Hubei Province and its zircon SHRIMP U-Pb age. Chinese Science Bulletin 54, 1058-1064. https://doi.org/10.1007/s11434-008-0589-6.

Liu, P., Xiao, S., Yin, C., Chen, S., Zhou, C., Li, M., 2014. Ediacaran acanthomorphic acritarchs and other microfossils from chert nodules of the upper Doushantuo Formation in the Yangtze Gorges area, South China. Journal of Paleontology 88 (supplement to No. 1), 1-139. https://doi.org/10.1666/13-009.

McFadden, K.A., Xiao, S., Zhou, C., Kowalewski, M., 2009. Quantitative evaluation of the biostratigraphic distribution of acanthomorphic acritarchs in the Ediacaran Doushantuo Formation in the Yangtze Gorges area, South China. Precambrian Research 173, 170-190.

McFadden, K.A., Huang, J., Chu, X., Jiang, G., Kaufman, A.J., Zhou, C., Yuan, X., Xiao, S., 2008. Pulsed oxidation and biological evolution in the Ediacaran Doushantuo Formation. Proceedings of the National Academy of Sciences 105, 3197-3202. https://doi.org/10.1073/pnas.0708336105.

Meister, P., Wiedling, J., Lott, C., Bach, W., Kuhfuß, H., Wegener, G., Böttcher, M.E., Deusner, C., Lichtschlag, A., Bernasconi, S.M., Weber, M., 2018. Anaerobic methane oxidation inducing carbonate precipitation at abiogenic methane seeps in the Tuscan archipelago (Italy). PLoS ONE 13, e0207305. https://doi.org/10.1371/journal.pone.0207305.

Rothman, D.H., Hayes, J.M., Summons, R., 2003. Dynamics of the Neoproterozoic carbon cycle. Proceedings of the National Academy of Sciences, USA 100, 8124-8129.

Saylor, B.Z., Kaufman, A.J., Grotzinger, J.P., Urban, F., 1998. A composite reference section for terminal Proterozoic strata of southern Namibia. Journal of Sedimentary Research, Section B: Stratigraphy and Global Studies 66, 1223-1235.

Schmitz, M.D., 2012. Appendix 2—Radiometric ages used in GTS2012, in: Gradstein, F., Ogg, J., Schmitz, M.D. , Ogg, G. (Editors), The Geologic Time Scale 2012. Elsevier, Boston, pp. 1045–1082.

Schrag, D.P., Higgins, J.A., Macdonald, F.A., Johnston, D.T., 2013. Authigenic carbonate and the history of the global carbon cycle. Science 339, 540-543. https://doi.org/10.1126/science.1229578.

Shields, G.A., Mills, B.J.W., Zhu, M., Raub, T.D., Daines, S.J., Lenton, T.M., 2019. Unique Neoproterozoic carbon isotope excursions sustained by coupled evaporite dissolution and pyrite burial. Nature Geoscience 12, 823-827. https://doi.org/10.1038/s41561-019-0434-3.

Śliwiński, M.G., Kitajima, K., Kozdon, R., Spicuzza, M.J., Fournelle, J.H., Denny, A., Valley, J.W., 2016a. Secondary ion mass spectrometry bias on isotope ratios in dolomite–ankerite, Part I: $\delta^{18}O$ matrix effects. Geostandards and Geoanalytical Research 40, 157–172. https://doi.org/10.1111/j.1751-908X.2015.00364.x.

Śliwiński, M.G., Kitajima, K., Kozdon, R., Spicuzza, M.J., Fournelle, J.H., Denny, A., Valley, J.W., 2016b. Secondary ion mass spectrometry bias on isotope ratios in dolomite–ankerite, Part II: $\delta^{13}C$ matrix effects. Geostandards and Geoanalytical Research 40, 173–184. https://doi.org/10.1111/j.1751-908X.2015.00380.x.

Sui, Y., Huang, C., Zhang, R., Wang, Z., Ogg, J., Kemp, D.B., 2018. Astronomical time scale for the lower Doushantuo Formation of early Ediacaran, South China. Science Bulletin 63, 1485-1494. https://doi.org/10.1016/j.scib.2018.10.010.

Sun, X., Turchyn, A.V., 2014. Significant contribution of authigenic carbonate to marine carbon burial. Nature Geoscience 7, 201-204. https://doi.org/10.1038/NGEO2070.

Swart, P.K., 2008. Global synchronous changes in the carbon isotopic composition of carbonate sediments unrelated to changes in the global carbon cycle. Proceedings of the National Academy of Sciences of the United States of America 105, 13741-13745. https://doi.org/10.1073/pnas.0802841105.

Tahata, M., Ueno, Y., Ishikawa, T., Sawaki, Y., Murakami, K., Han, J., Shu, D., Li, Y., Guo, J., Yoshida, N., Komiya, T., 2013. Carbon and oxygen isotope chemostratigraphies of the Yangtze platform, South China: Decoding temperature and environmental changes through the Ediacaran. Gondwana Research 23, 333-353. https://doi.org/10.1016/j.gr.2012.04.005.

Tostevin, R., Wood, R.A., Shields, G.A., Poulton, S.W., Guilbaud, R., Bowyer, F., Penny, A.M., He, T., Curtis, A., Hoffmann, K.H., Clarkson, M.O., 2016. Low-oxygen waters limited habitable space for early animals. Nature Communications 7, 12818. https://doi.org/10.1038/ncomms12818.

Turnier, R.B., Katzir, Y., Kitajima, K., Orland, I.J., Spicuzza, M.J., Valley, J.W., 2020. Calibration of oxygen isotope fractionation and calcite‐corundum thermometry in emery at Naxos, Greece. Journal of Metamorphic Petrology 38, 53-70. https://doi.org/10.1111/jmg.12512.

Valley, J.W., Kita, N.T., 2009. In situ oxygen isotope geochemistry by ion microprobe, in: Fayek, M. (Editor), MAC Short Course: Secondary Ion Mass Spectrometry in the Earth Sciences, pp. 19-63.

Vickers-Rich, P., Narbonne, G.M., Laflamme, M., Darroch, S.A.F., Kaufman, A.J., Kriesfeld, L., 2016. The Nama Group of southern Namibia. 35th International Geological Congress Pre-conference Field Guide, 1-74.

Wang, J., Jiang, G., Xiao, S., Li, Q., Wei, Q., 2008. Carbon isotope evidence for widespread methane seeps in the ~635 Ma Doushantuo cap carbonate in South China. Geology 36, 347-350.

Wang, Z., Wang, J., Kouketsu, Y., Bodnar, R.J., Gill, B.C., Xiao, S., 2017. Raman geothermometry of carbonaceous material in the basal Ediacaran Doushantuo cap dolostone: the thermal history of extremely negative $\delta^{13}C$ signatures in the aftermath of the terminal Cryogenian snowball Earth glaciation. Precambrian Research 298, 174-186. https://doi.org/10.1016/j.precamres.2017.06.013.

Wood, R.A., Poulton, S.W., Prave, A.R., Hoffmann, K.H., Clarkson, M.O., Guilbaud, R., Lyne, J.W., Tostevin, R., Bowyer, F., Penny, A.M., Curtis, A., Kasemann, S.A., 2015. Dynamic redox conditions control late Ediacaran metazoan ecosystems in the Nama Group, Namibia. Precambrian Research 261, 252-271. https://doi.org/10.1016/j.precamres.2015.02.004.

Xiao, S., 2004. New multicellular algal fossils and acritarchs in Doushantuo chert nodules (Neoproterozoic, Yangtze Gorges, South China). Journal of Paleontology 78, 393-401.

Xiao, S., Knoll, A.H., Yuan, X., Pueschel, C.M., 2004. Phosphatized multicellular algae in the Neoproterozoic Doushantuo Formation, China, and the early evolution of florideophyte red algae. American Journal of Botany 91, 214-227.

Xiao, S., Schiffbauer, J.D., McFadden, K.A., Hunter, J., 2010. Petrographic and SIMS pyrite sulfur isotope analyses of Ediacaran chert nodules: Implications for microbial processes in pyrite rim formation, silicification, and exceptional fossil preservation. Earth and Planetary Science Letters 297, 481–495. https://doi.org/10.1016/j.epsl.2010.07.001.

Xiao, S., Bykova, N., Kovalick, A., Gill, B.C., 2017. Stable carbon isotopes of sedimentary kerogens and carbonaceous macrofossils from the Ediacaran Miaohe Member in South China: Implications for stratigraphic correlation and sources of sedimentary organic carbon. Precambrian Research 302, 171-179. https://doi.org/10.1016/j.precamres.2017.10.006.

Xiao, S., McFadden, K.A., Peek, S., Kaufman, A.J., Zhou, C., Jiang, G., Hu, J., 2012. Integrated chemostratigraphy of the Doushantuo Formation at the northern Xiaofenghe section (Yangtze Gorges, South China) and its implication for Ediacaran stratigraphic correlation and ocean redox models. Precambrian Research 192-95, 125-141. https://doi.org/10.1016/j.precamres.2011.10.021.

Xiao, S., Narbonne, G.M., Zhou, C., Laflamme, M., Grazhdankin, D.V., Moczydłowska-Vidal, M., Cui, H., 2016. Toward an Ediacaran time scale: problems, protocols, and prospects. Episodes 39, 540–555. https://doi.org/10.18814/epiiugs/2016/v39i4/103886.

Zhang, Y., Yin, L., Xiao, S., Knoll, A.H., 1998. Permineralized fossils from the terminal Proterozoic Doushantuo Formation, South China. Journal of Paleontology 72 (supplement to No. 4), 1-52.

Zhou, C., Xiao, S., 2007. Ediacaran $\delta^{13}C$ chemostratigraphy of South China. Chemical Geology 237, 89-108.

Zhou, C., Bao, H., Peng, Y., Yuan, X., 2010. Timing the deposition of ^{17}O-depleted barite at the aftermath of Nantuo glacial meltdown in South China. Geology 38, 903-906. https://doi.org/10.1130/G31224.1.

Zhou, C., Guan, C., Cui, H., Ouyang, Q., Wang, W., 2016. Methane-derived authigenic carbonate from the lower Doushantuo Formation of South China: Implications for seawater sulfate concentration and global carbon cycle in the early Ediacaran ocean. Palaeogeography Palaeoclimatology Palaeoecology 461, 145–155. https://doi.org/10.1016/j.palaeo.2016.08.017.

Zhou, C., Xiao, S., Wang, W., Guan, C., Ouyang, Q., Chen, Z., 2017a. The stratigraphic complexity of the middle Ediacaran carbon isotopic record in the Yangtze Gorges area, South China, and its implications for the age and chemostratigraphic significance of the Shuram excursion. Precambrian Research 288, 23-38. https://doi.org/10.1016/j.precamres.2016.11.007.

Zhou, C., Li, X.-H., Xiao, S., Lan, Z., Ouyang, Q., Guan, C., Chen, Z., 2017b. A new SIMS zircon U-Pb date from the Ediacaran Doushantuo Formation: age constraint on the Weng'an biota. Geological Magazine 154, 1193-1201. https://doi.org/10.1017/S0016756816001175.

Zhu, M., Lu, M., Zhang, J., Zhao, F., Li, G., Yang, A., Zhao, X., Zhao, M., 2013. Carbon isotope chemostratigraphy and sedimentary facies evolution of the Ediacaran Doushantuo Formation in western Hubei, South China. Precambrian Research 225, 7-28. https://doi.org/10.1016/j.precamres.2011.07.019.

Figure Captions

Figure 1. Bulk-sample $\delta^{13}C_{carb}$ profile of the Ediacaran Doushantuo Formation at the Jiulongwan section (30°48'12.72"N, 111°03'20.70"E) in the Yangtze Gorges area of South China, illustrating noisy stratigraphic variation in lower member II of the formation (ca. 4–35 meters in stratigraphic height). Inset maps show major tectonic units in China and the location of the Jiulongwan section (red dot) in the Yangtze Craton. $\delta^{13}C$ data are compiled from Jiang et al. (2007), McFadden et al. (2008), Tahata et al. (2013), and new data generated in this study. The McFadden et al. (2008) dataset includes measurements made at University of Maryland and Chinese Academy of Sciences, which are plotted separately. Data from Tahata et al. (2013) were from a drill core about 3 km from Jiulongwan and are rescaled according to lithostratigraphic correlation (see Supplementary Data 1). Three samples from McFadden et al. (2008), JLW15.1, JLW23.5, and JLW35.2 (red arrows) were selected for SIMS $\delta^{13}C$ analysis. Radiometric ages are from the Yangtze Gorges area published by Condon et al. (2005) unless otherwise noted. Radiometric ages marked by solid dots can be placed in the Jiulongwan section with confidence. The 614±7.6 Ma and 609±5 Ma ages are from the Zhangcunping area about 70 km to the northeast of the Jiulongwan section (Liu et al., 2009; Zhou et al., 2017b). Note that the 551.1±0.7 Ma age was from the uppermost Miaohe Member that has been variously correlated with Member IV of the Doushantuo Formation (Xiao et al., 2017; Zhou et al., 2017a) or the Shibantan Member of the Dengying Formation (An et al., 2015). The new data show a weaker and shorter EN2 (–3.2‰ at 68.5 m) than previously published data. The origin of this discrepancy is uncertain but may be related to the fact that the different studies sampled the Jiulongwan section independently, the Jiulongwan section consists of two sub-sections that were spliced near the Member II–III boundary (i.e., part of EN2 may not be sampled in our study), and stratigraphic

scaling of the different studies may not be accurate (which may have also resulted in the discrepancy at 110–115 m).

Fig. 2. Bulk-sample $\delta^{13}C_{carb}$ profile of the Ediacaran Mooifontein Member (highlighted) of the Zaris Formation at the Arasab section near Farm Aar and ~20 km south of Aus in southern Namibia. Map of Namibia modified from Hall et al. (2013). Stratocolumn and $\delta^{13}C_{carb}$ data are from Wood et al. (2015). See Supplementary Data 2.

Figure 3. Field and thin-section petrographic photographs. (a) Field photograph of chert nodules in the lower Member II of the Doushantuo Formation at the Huajipo section about 5 km southwest of the Jiulongwan section. (b–c) Petrographic thin sections of chert nodules from samples XF141 and JLW15.1, respectively. Note that XF141 is not one of the samples analyzed in this study; it is from Member II of the Doushantuo Formation at the Xiaofenghe section, about 22 km northeast of the Jiulongwan section. Silica core, pyrite rim, calcite rim, warping laminae, and dolomite matrix are marked in (a–c). (d) Field photograph of the Mooifontein Member near Farm Aar, showing the abundance of *Cloudina* fossils preserved as internal molds. (e–f) Plane light and differential interference contrast (DIC) microscopic images, respectively, of *Cloudina* specimens in a petrographic thin section of the Mooifontein sample 2016AarFarm analyzed in this study. The two images illustrate approximately the same area, with slightly different orientations and magnifications. White circle and paired arrows mark three *Cloudina* specimens in transverse and longitudinal cross sections, respectively. Note the coarse-grained recrystallized calcite minerals and the moldic preservation of *Cloudina*.

Figure 4. SIMS $\delta^{13}C$ data of JLW15.1A, a subsample of JLW15.1. (a) Reflected light microscopic photo montage of the sample, with labeled rectangles denoting areas or domains for SIMS and EPMA analyses. Calcite (Cal), dolomite (Dol), pyrite (Py), Quartz (Qz), and anthracite (An) standards were mounted on the sample and polished for SIMS and EPMA analyses. (b–d) Backscattered electron microscopic images of domains 1–3, respectively, which are marked in (a). Major minerals (dolomite, calcite, pyrite, and silica), SIMS spots, and corresponding $\delta^{13}C$ measurements (yellow: calcite measurements) are marked on the figure. The spot-to-spot precision of $\delta^{13}C$ values based on all bracketing analyses on standard UWC-3 is ±0.6‰ (2SD; see Supplementary Data 3).

Figure 5. SIMS $\delta^{13}C$ data of JLW15.1A mapped on cathodoluminescence (CL) images. (a–c) CL images corresponding to Fig. 4b–d. (d) Magnified view of central part of (c).

Fig. 6. SIMS $\delta^{13}C$ data of sample JLW15.1B, a subsample of JLW15.1. (a) Reflected light microscopic photo montage of the sample, with labeled rectangles denoting areas or domains for SIMS and EPMA analyses. Calcite (Cal), dolomite (Dol), pyrite (Py), Quartz (Qz), and anthracite (An) standards were mounted on the sample and polished for SIMS and EPMA analyses. (b–d) Backscattered electron microscopic images of domains 1–3, respectively, which are marked in (a). Major minerals (dolomite, calcite, pyrite, and silica), SIMS spots, and corresponding $\delta^{13}C$ measurements (yellow: calcite measurements) are marked on the figure. The

spot-to-spot precision of δ^{13}C values based on all bracketing analyses on standard UWC-3 is ±0.6‰ (2SD; see Supplementary Data 3).

Figure 7. SIMS δ^{13}C data of JLW15.1B mapped on cathodoluminescence (CL) images. (a), (b–c), and (d) are CL images corresponding to Fig. 6b–d, respectively.

Figure 8. SIMS δ^{13}C data of sample JLW23.5. (a) Reflected light microscopic photo montage of the sample, with labeled rectangles denoting areas or domains for SIMS and EPMA analyses. Calcite (Cal), dolomite (Dol), pyrite (Py), Quartz (Qz), and anthracite (An) standards were mounted on the sample and polished for SIMS and EPMA analyses. (b–f) Backscattered electron microscopic images of domains 1–4 marked in (a). (c) is a magnified view of rectangle in (b). Major minerals (dolomite, calcite, pyrite, and silica), SIMS spots, and corresponding δ^{13}C measurements (yellow: calcite measurements; blue: dolomite measurements) are marked on the figure. The spot-to-spot precision of δ^{13}C values based on all bracketing analyses on standard UWC-3 is ±0.6‰ (2SD; see Supplementary Data 3).

Figure 9. SIMS δ^{13}C data of JLW23.5 mapped on cathodoluminescence (CL) images. (a) CL image corresponding to Fig. 8b (upper), (b) to Fig. 8c (lower right), (c) to Fig. 8c (central left), (d) to Fig. 8d, (f) to Fig. 8e (left), (g) to Fig. 8e (right, and (h) to Fig. 8f. (e) is magnified view of lower right of (d), showing calcite cement (central right) in dolomitic matrix. Note the presence of multiple CL colors in dolomitic matrix, indicating the presence of multiple phases of carbonate minerals including authigenic carbonate.

Figure 10. SIMS $\delta^{13}C$ data of sample JLW35.2. (a) Reflected light microscopic photo montage of the sample, with labeled rectangles denoting areas or domains for SIMS and EPMA analyses. Calcite (Cal), dolomite (Dol), pyrite (Py), Quartz (Qz), and anthracite (An) standards were mounted on the sample and polished for SIMS and EPMA analyses. (b–f) Backscattered electron microscopic images of domains 1–5 marked in (a). (g) is a magnified view of rectangle in (f). Major minerals (dolomite, calcite, pyrite, and silica), SIMS spots, and corresponding $\delta^{13}C$ measurements (yellow: calcite measurements) are marked on the figure. OM, organic matter. The spot-to-spot precision of $\delta^{13}C$ values based on all bracketing analyses on standard UWC-3 is ±0.6‰ (2SD; see Supplementary Data 3).

Figure 11. SIMS $\delta^{13}C$ data of JLW35.2 mapped on cathodoluminescence (CL) images. (a) CL image corresponding to Fig. 10b, (b) to Fig. 10c, (d) to Fig. 10d, (e) to Fig. 10e, and (f) to Fig. 10f–g. (c) is magnified view of lower right of (b), showing calcite cement (central) in dolomitic matrix. (g) CL image of dolomitic matrix near area shown in (c). Note the presence of multiple CL colors in calcite/chert nodule (a, d, f), calcite cement (c, central), and dolomitic matrix (c, peripheral; g), indicating the presence of multiple phases of authigenic carbonate minerals.

Figure 12. SIMS $\delta^{13}C$ data of sample 16AarFarm. (a–b) Backscattered electron microscopic images with SIMS spots and corresponding $\delta^{13}C$ measurements (yellow: calcite measurements). Calcite is the dominant mineral in this sample. Light brown shading was added to mark the internal molds of two *Cloudina* tests in longitudinal and transverse cross-sections, respectively.

Calcite (Cal), dolomite (Dol), pyrite (Py), Quartz (Qz), and anthracite (An) standards were mounted on the sample and polished for SIMS and EPMA analyses. The spot-to-spot precision of $\delta^{13}C$ values based on all bracketing analyses on standard UWC-3 is ±0.6‰ (2SD; see Supplementary Data 3).

Figure 13. SIMS $\delta^{13}C$ data of 16AarFarm mapped on cathodoluminescence (CL) images. (a-e) CL image corresponding to Fig. 12a (from left to right), and (f) to Fig. 12b.

Figure 14. Histograms and box-and-whisker diagrams of SIMS $\delta^{13}C$ measurements of the four analyzed samples. Each box-and-whisker plot shows the median, 1st and 3rd quartiles, range, and outliers (⩾3rd quartile + 1.5 * interquartile range, or ⩽1st quartile – 1.5 * interquartile range; denoted by circular dots). For comparison, bulk-sample $\delta^{13}C$ values of the same samples are denoted by green arrows, with values marked above; note that duplicate measurements were attempted for JLW15.1 and JLW23.5, and the green arrows point to the average of the duplicates. Additionally, stratigraphic variations in $\delta^{13}C$ at meter scales are marked by red double-arrowed lines, with ranges of $\delta^{13}C$ values annotated above.

Figure 15. SIMS $\delta^{13}C$ measurements plotted against sample numbers (a), fabrics (b), and EPMA elemental geochemical data (c–f). $\delta^{13}C$ measurements of calcite are represented by open circles, and four analyses of dolomite by circles filled with gray. Arrows in (a) mark bulk-sample measurements.

Supplementary Data 1. Bulk sample $\delta^{13}C_{carb}$ data of the Doushantuo Formation at the Jiulongwan section from Jiang et al. (2007), McFadden et al. (2008), Tahata et al. (2013), as well as new data generated in this study. Data are plotted in Fig. 1.

Supplementary Data 2. Bulk sample $\delta^{13}C_{carb}$ data of the Mooifontein Member at the Arasab section near Farm Aar in the Witpus sub-basin of southern Namibia (Wood et al., 2015), as well as a new analysis of sample 2016AarFarm from the Mooifontein Member at Farm Aar. Data are plotted in Fig. 2.

Supplementary Data 3. SIMS $\delta^{13}C_{carb}$ data and EPMA data of three Doushantuo samples (JLW-15.1, JLW-23.5, and JLW-35.2) and one Mooifontein sample (2016AarFarm). Data are plotted in Figs. 4–15.

Supplementary Data 4. Post-SIMS secondary electron SEM images of three Doushantuo samples (JLW-15.1, JLW-23.5, and JLW-35.2) and one Mooifontein sample (2016AarFarm). SIMS pits are circled and labeled with analysis numbers (corresponding to analysis numbers in Supplementary Data 3, sheet "SIMS Data") and $\delta^{13}C$ values (in ‰ VPDB). If a SIMS pit is not circled or labeled, the analysis was not good (marked by strike-through text in Supplementary Data 3). Data are also mapped on BSE and CL images in Figs. 4–13.

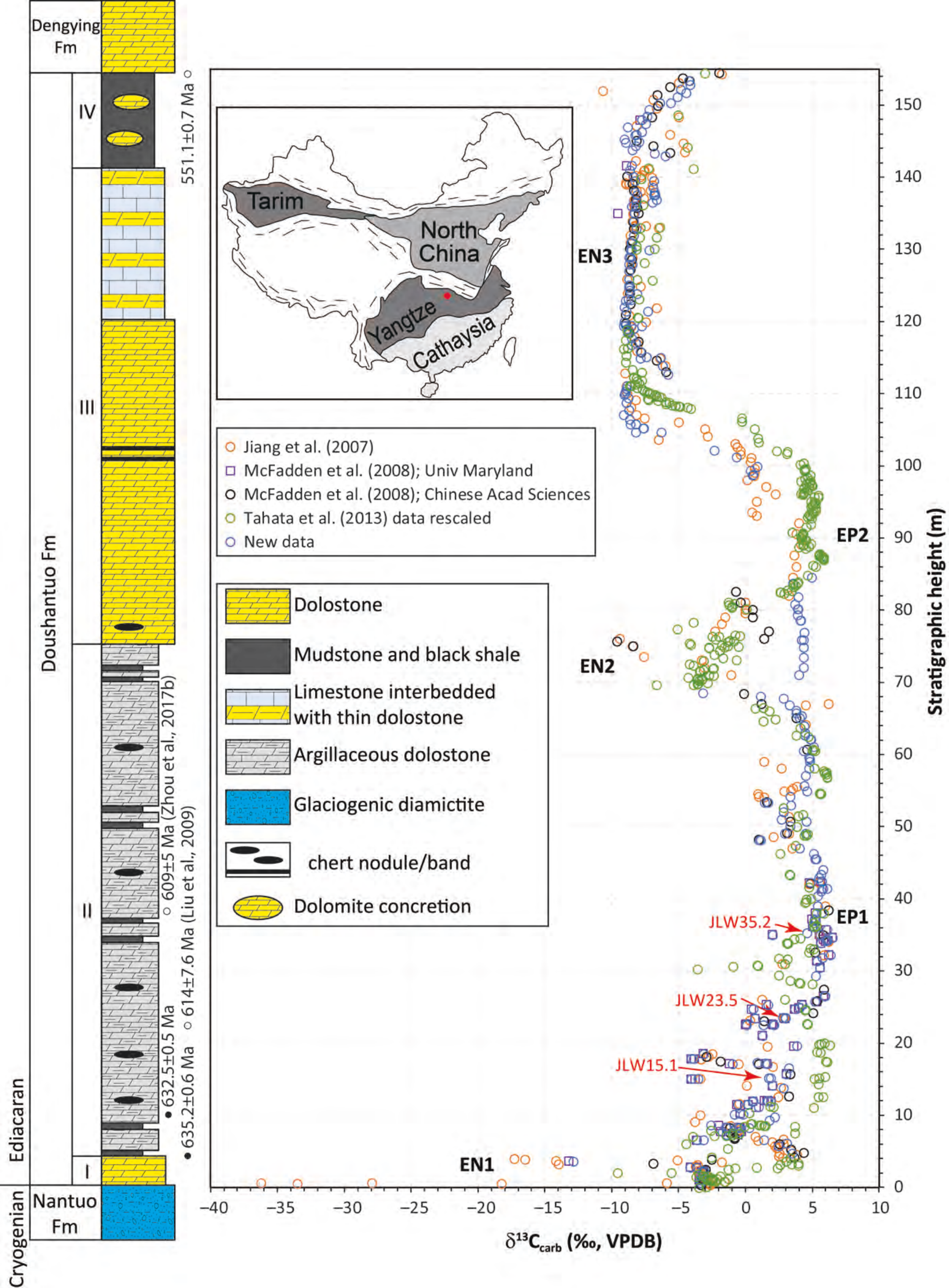
Dengying Fm
IV
551.1±0.7 Ma
III
Doushantuo Fm
II
609±5 Ma (Zhou et al., 2017b)
614±7.6 Ma (Liu et al., 2009)
632.5±0.5 Ma
635.2±0.6 Ma
I
Ediacaran
Nantuo Fm
Cryogenian
Tarim
North China
Yangtze
Cathaysia
Jiang et al. (2007)
McFadden et al. (2008); Univ Maryland
McFadden et al. (2008); Chinese Acad Sciences
Tahata et al. (2013) data rescaled
New data
Dolostone
Mudstone and black shale
Limestone interbedded with thin dolostone
Argillaceous dolostone
Glaciogenic diamictite
chert nodule/band
Dolomite concretion
EN3
EN2
EN1
EP2
EP1
JLW35.2
JLW23.5
JLW15.1
−40
−35
−30
−25
−20
−15
−10
−5
0
5
10
δ13Ccarb (‰, VPDB)
0
10
20
30
40
50
60
70
80
90
100
110
120
130
140
150
Stratigraphic height (m)

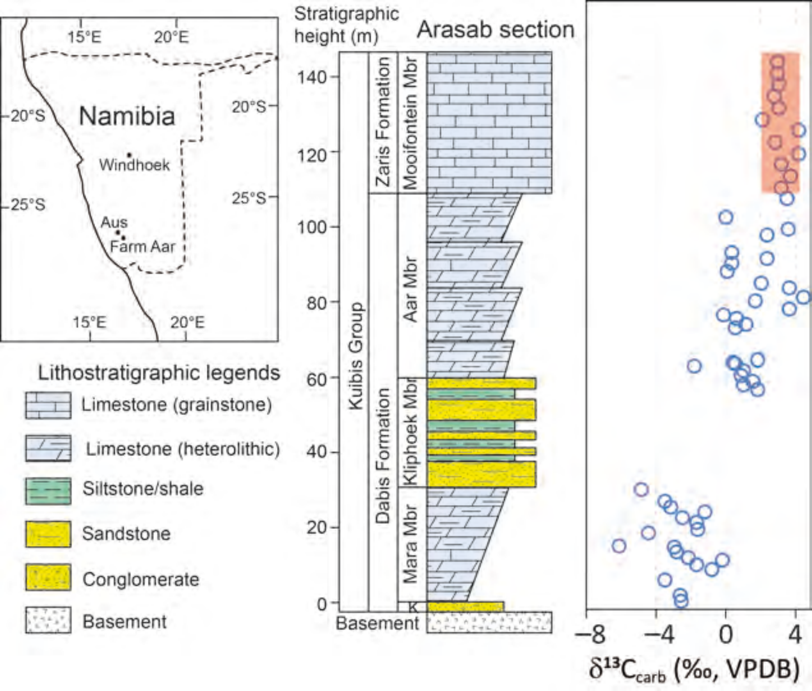
15°E
20°E
20°S
20°S
Namibia
Windhoek
25°S
25°S
Aus
Farm Aar
15°E
20°E
Lithostratigraphic legends
Limestone (grainstone)
Limestone (heterolithic)
Siltstone/shale
Sandstone
Conglomerate
Basement
Stratigraphic height (m)
Arasab section
140
120
100
80
60
40
20
0
Kuibis Group
Zaris Formation
Dabis Formation
Mooifontein Mbr
Aar Mbr
Kliphoek Mbr
Mara Mbr
K
Basement
−8
−4
0
4
δ13Ccarb (‰, VPDB)

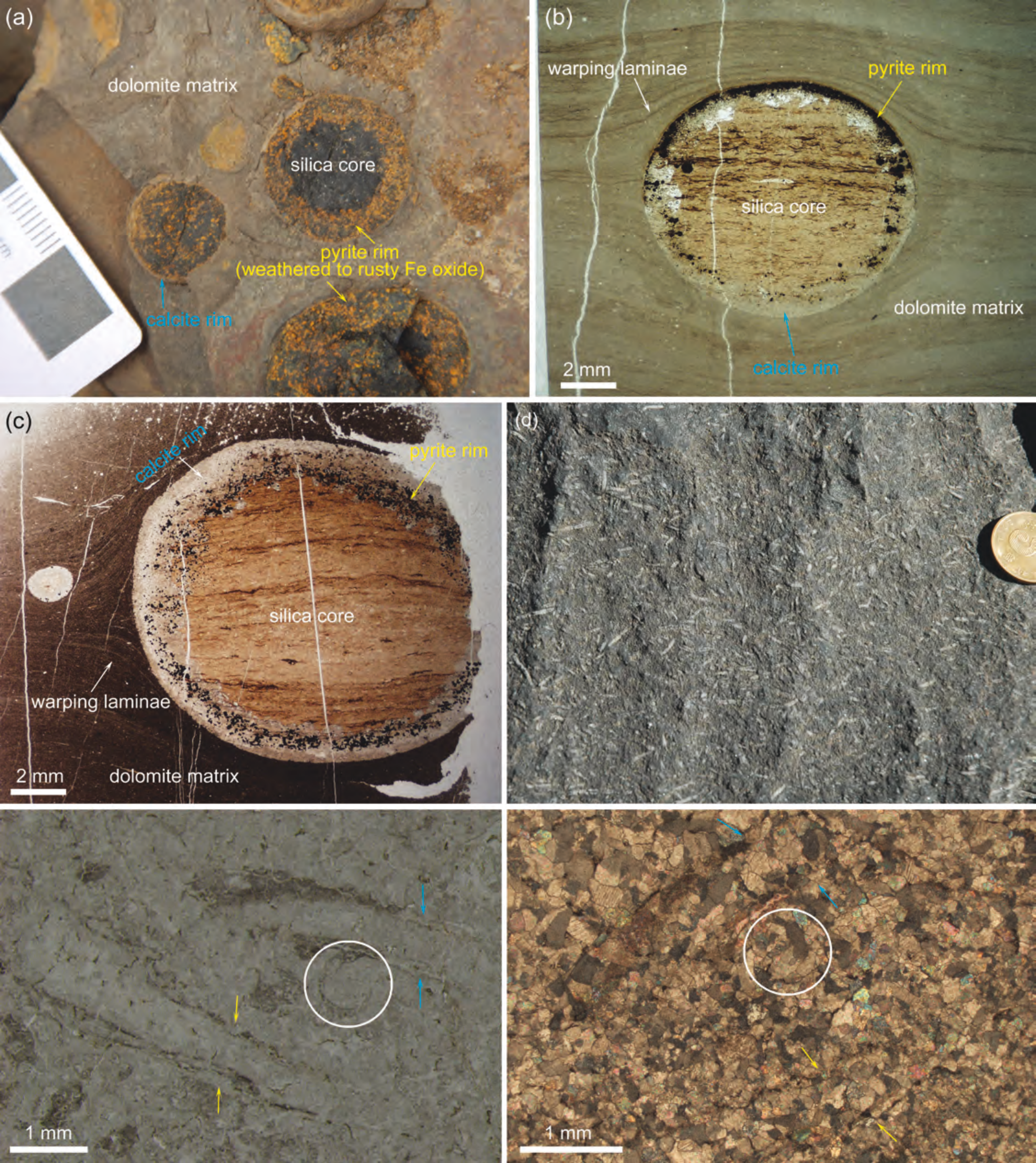
(a)
dolomite matrix
silica core
pyrite rim
(weathered to rusty Fe oxide)
calcite rim
(b)
warping laminae
pyrite rim
silica core
dolomite matrix
2 mm
calcite rim
(c)
calcite rim
pyrite rim
silica core
warping laminae
2 mm
dolomite matrix
(d)
1 mm
1 mm

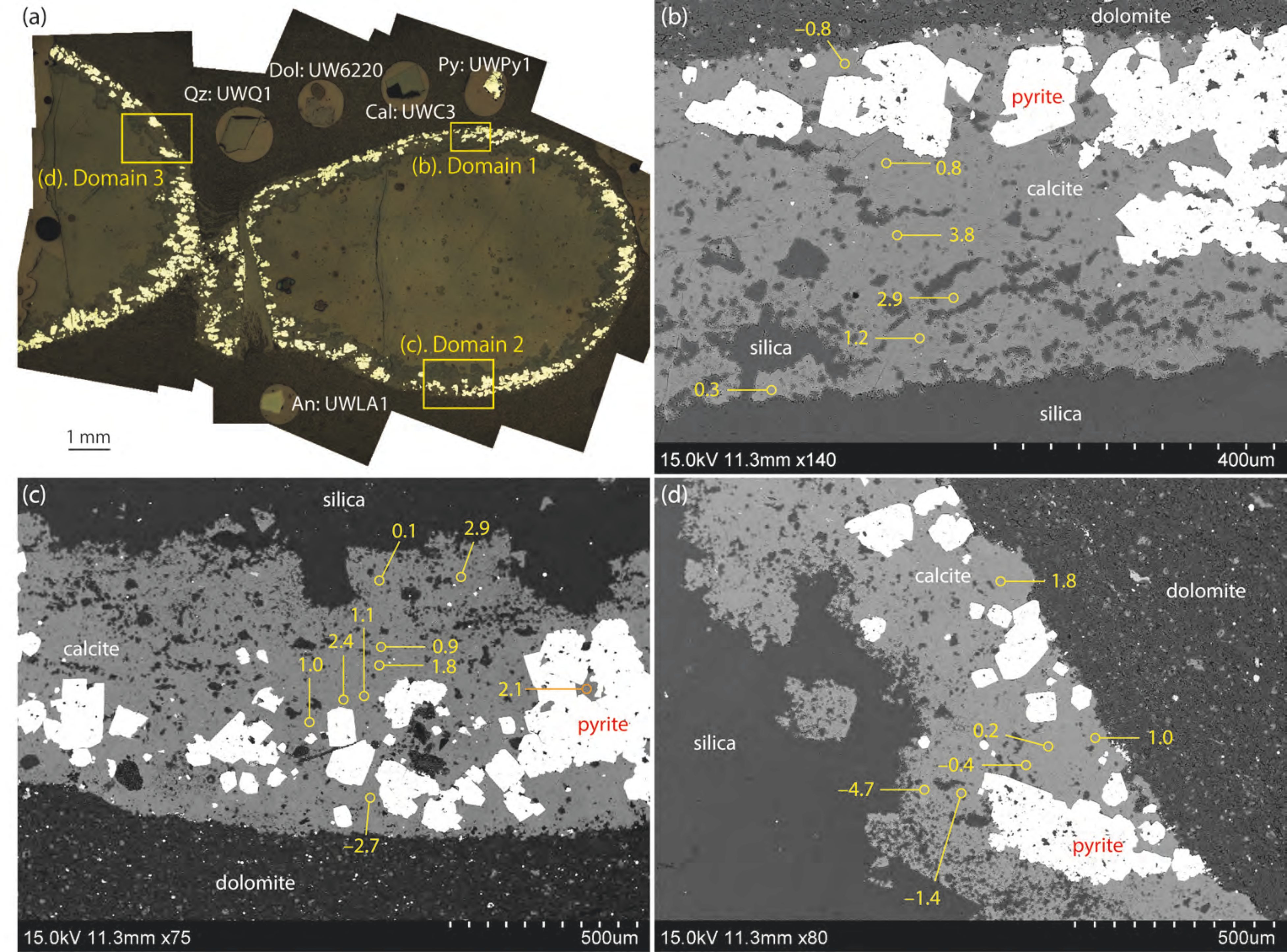
(a)
Dol: UW6220
Py: UWPy1
Qz: UWQ1
Cal: UWC3
(d). Domain 3
(b). Domain 1
(c). Domain 2
An: UWLA1
1 mm
(b)
dolomite
−0.8
pyrite
0.8
calcite
3.8
2.9
1.2
silica
0.3
silica
15.0kV 11.3mm x140
400um
(c)
silica
0.1
2.9
1.1
2.4
0.9
1.8
1.0
calcite
2.1
pyrite
−2.7
dolomite
15.0kV 11.3mm x75
500um
(d)
calcite
1.8
dolomite
silica
0.2
1.0
−0.4
−4.7
−1.4
pyrite
15.0kV 11.3mm x80
500um

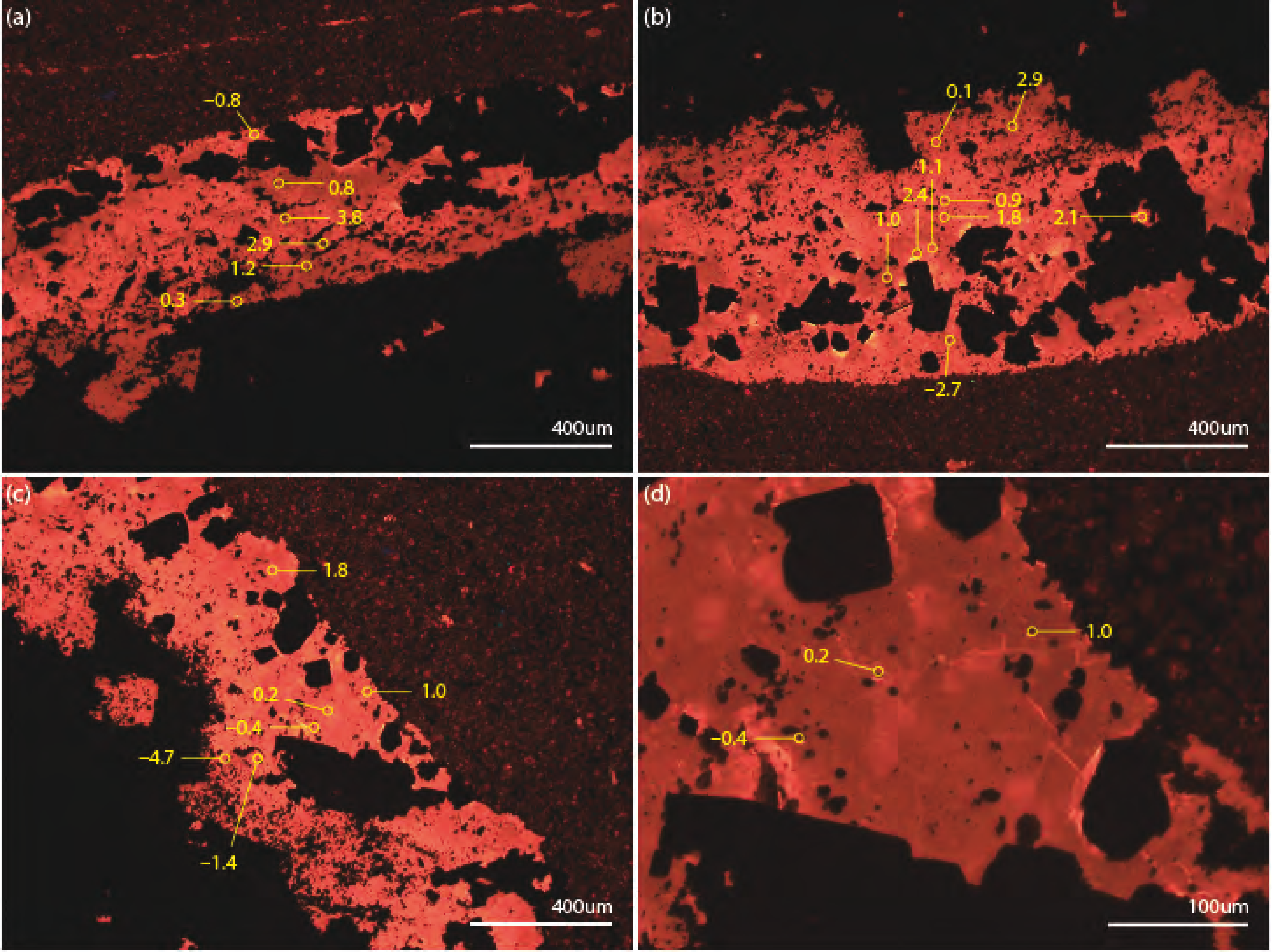
(a)
−0.8
0.8
3.8
2.9
1.2
0.3
400um
(b)
0.1
2.9
1.1
2.4
0.9
1.0
1.8
2.1
−2.7
400um
(c)
1.8
1.0
0.2
−0.4
−4.7
−1.4
400um
(d)
1.0
0.2
−0.4
100um

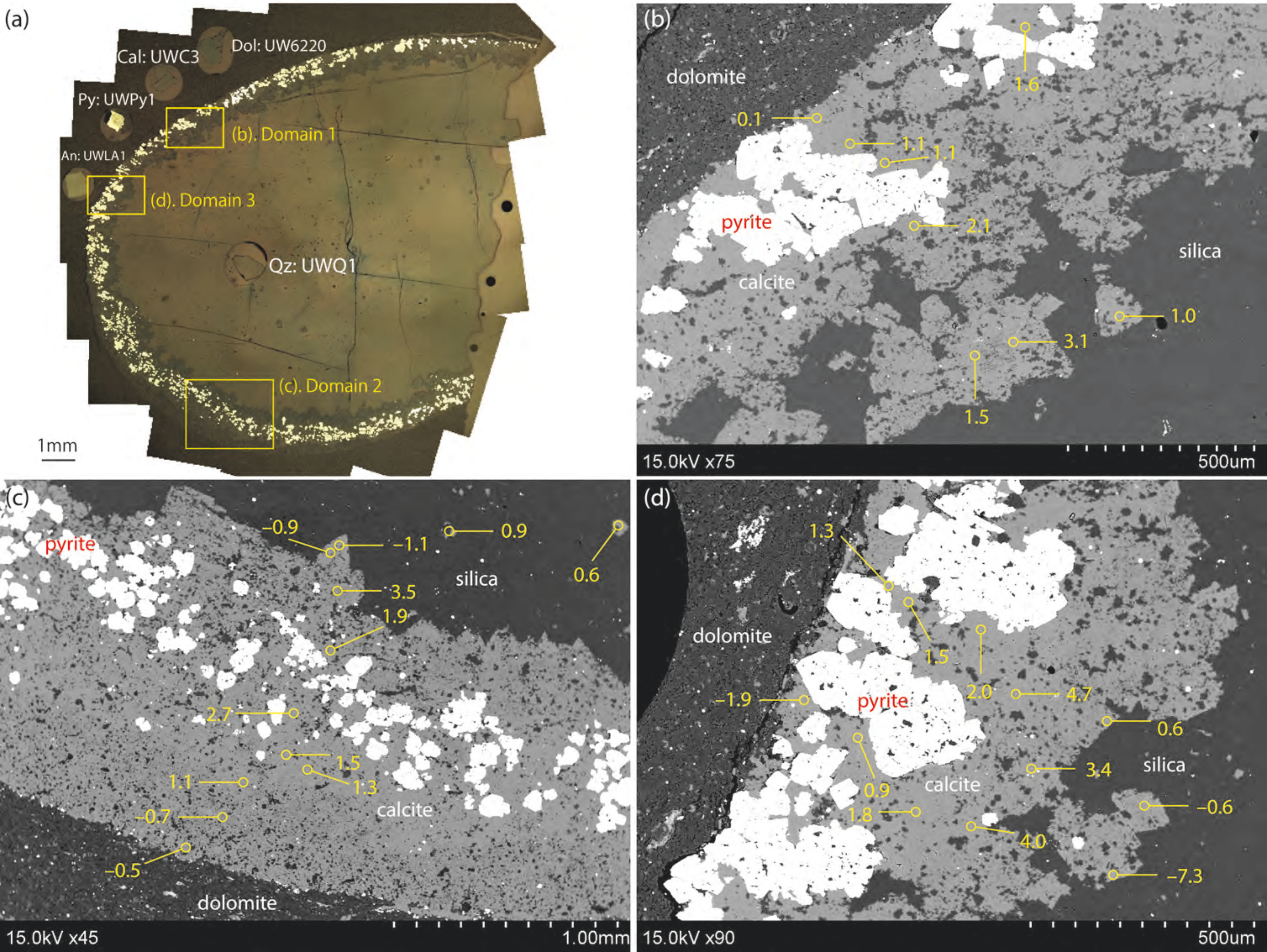
(a)
Cal: UWC3
Dol: UW6220
Py: UWPy1
An: UWLA1
(b). Domain 1
(d). Domain 3
Qz: UWQ1
(c). Domain 2
1mm
(b)
dolomite
1.6
0.1
1.1
1.1
pyrite
2.1
silica
calcite
1.0
3.1
1.5
15.0kV x75
500um
(c)
pyrite
–0.9
–1.1
0.9
0.6
silica
3.5
1.9
2.7
1.5
1.3
1.1
–0.7
calcite
–0.5
dolomite
15.0kV x45
1.00mm
(d)
1.3
dolomite
1.5
2.0
–1.9
pyrite
4.7
0.6
3.4
silica
calcite
0.9
1.8
–0.6
4.0
–7.3
15.0kV x90
500um

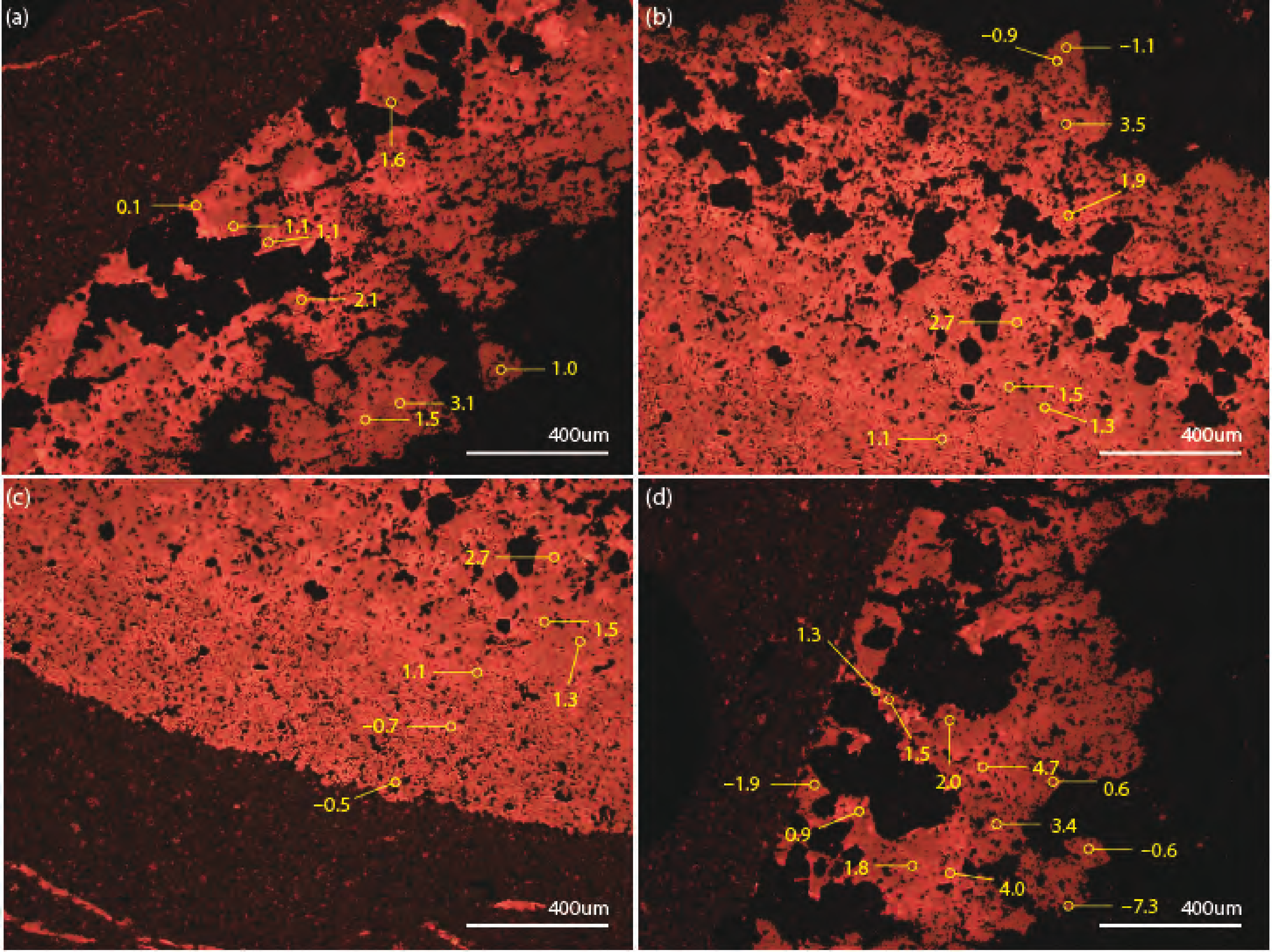
(a)
1.6
0.1
1.1
1.1
2.1
1.0
3.1
1.5
400um
(b)
−0.9
−1.1
3.5
1.9
2.7
1.5
1.3
1.1
400um
(c)
2.7
1.5
1.3
1.1
−0.7
−0.5
400um
(d)
1.3
1.5
2.0
4.7
0.6
−1.9
3.4
0.9
−0.6
1.8
4.0
−7.3
400um

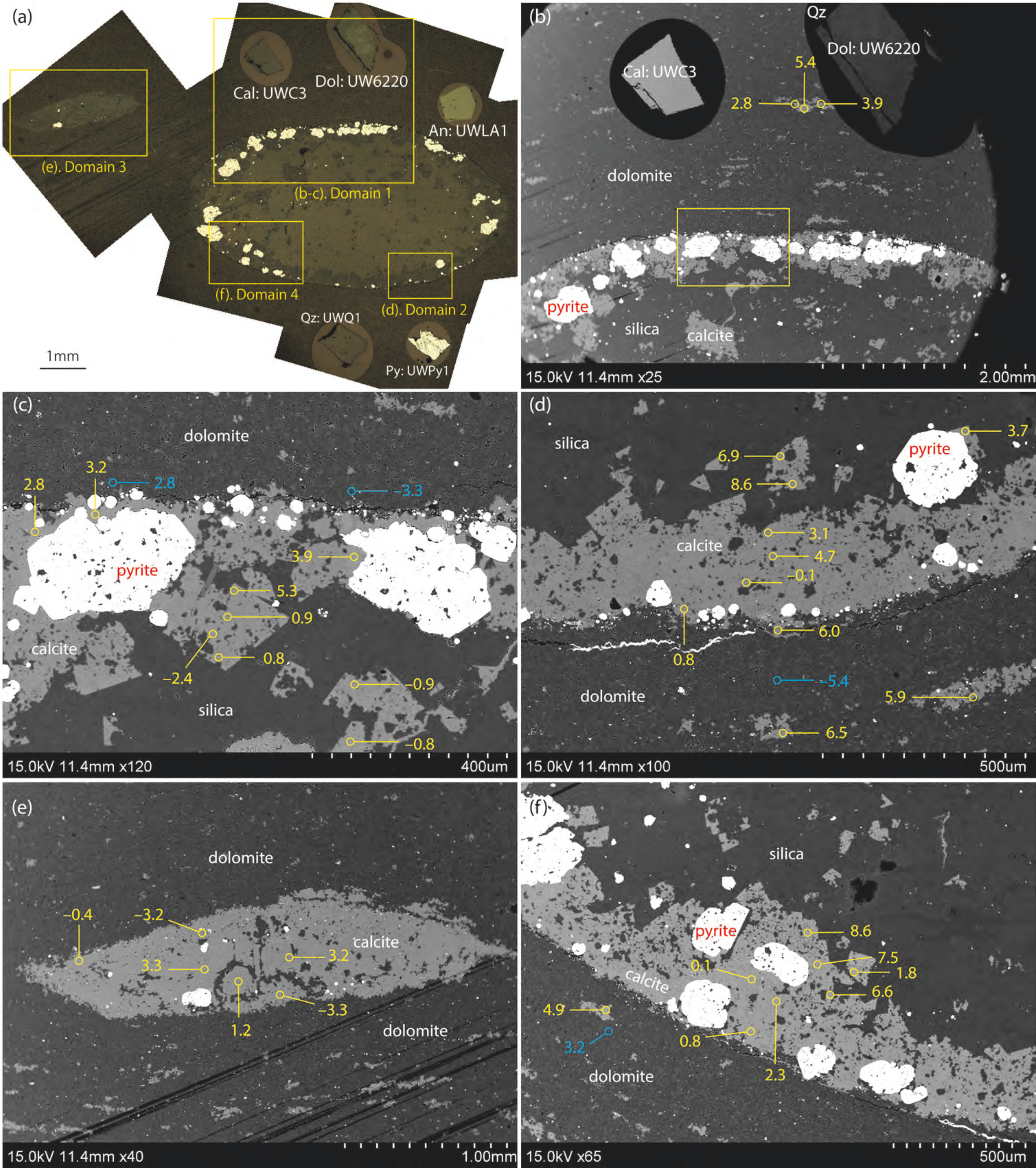
(a)
Cal: UWC3
Dol: UW6220
An: UWLA1
(e). Domain 3
(b-c). Domain 1
(f). Domain 4
(d). Domain 2
Qz: UWQ1
Py: UWPy1
1mm
(b)
Qz
Dol: UW6220
Cal: UWC3
5.4
2.8
3.9
dolomite
pyrite
silica
calcite
15.0kV 11.4mm x25
2.00mm
(c)
dolomite
3.2
2.8
2.8
−3.3
pyrite
3.9
5.3
0.9
calcite
−2.4
0.8
−0.9
silica
−0.8
15.0kV 11.4mm x120
400um
(d)
silica
6.9
8.6
3.7
pyrite
3.1
calcite
4.7
−0.1
6.0
0.8
−5.4
dolomite
5.9
6.5
15.0kV 11.4mm x100
500um
(e)
dolomite
−0.4
−3.2
calcite
3.3
3.2
1.2
−3.3
dolomite
15.0kV 11.4mm x40
1.00mm
(f)
silica
pyrite
8.6
7.5
0.1
1.8
calcite
6.6
4.9
3.2
0.8
2.3
dolomite
15.0kV x65
500um

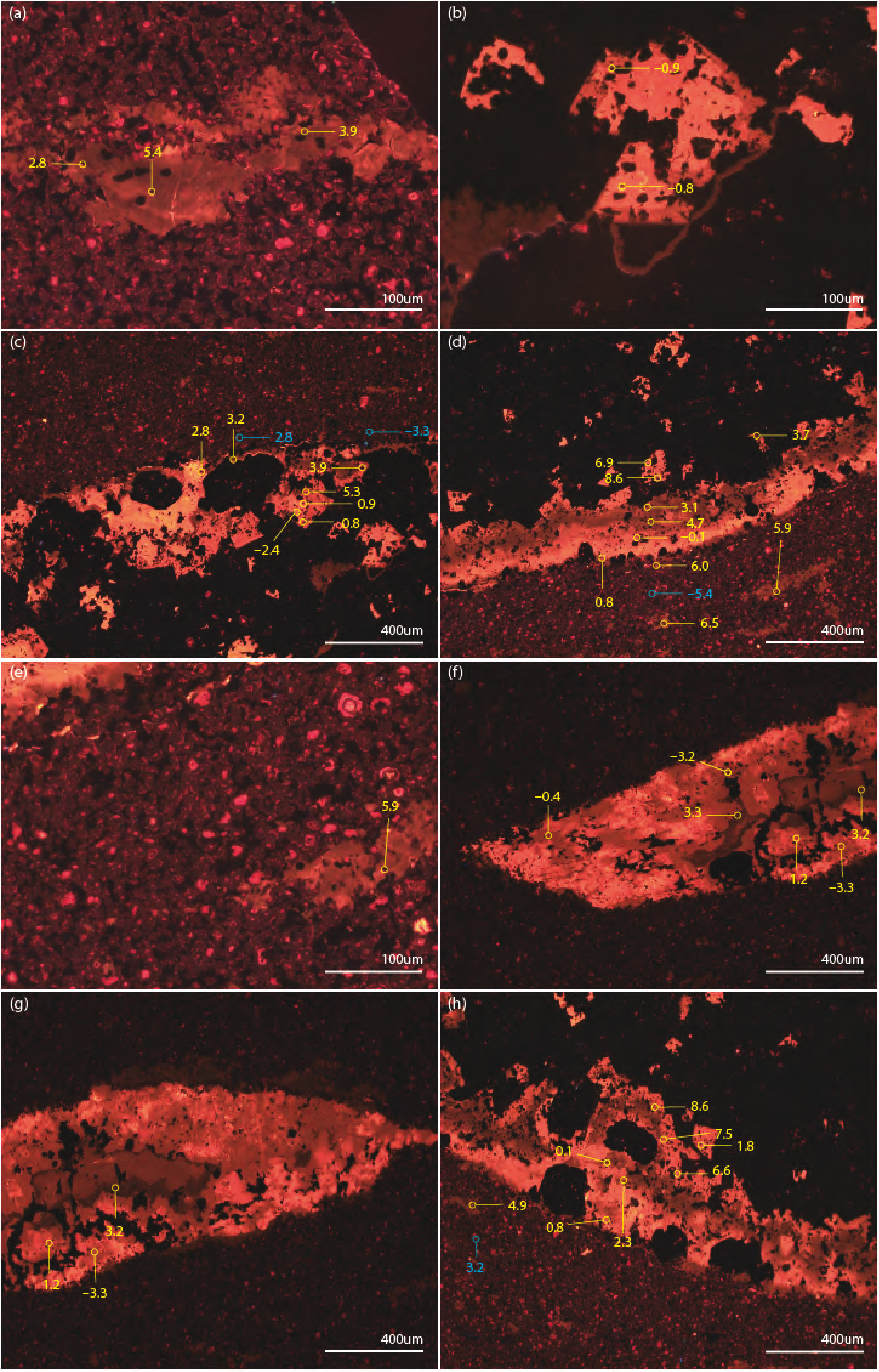
(a)
3.9
5.4
2.8
100um
(b)
−0.9
−0.8
100um
(c)
3.2
2.8
2.8
−3.3
3.9
5.3
0.9
0.8
−2.4
400um
(d)
3.7
6.9
8.6
3.1
4.7
−0.1
5.9
6.0
0.8
−5.4
6.5
400um
(e)
5.9
100um
(f)
−3.2
−0.4
3.3
3.2
1.2
−3.3
400um
(g)
3.2
1.2
−3.3
400um
(h)
8.6
7.5
1.8
0.1
6.6
4.9
0.8
2.3
3.2
400um

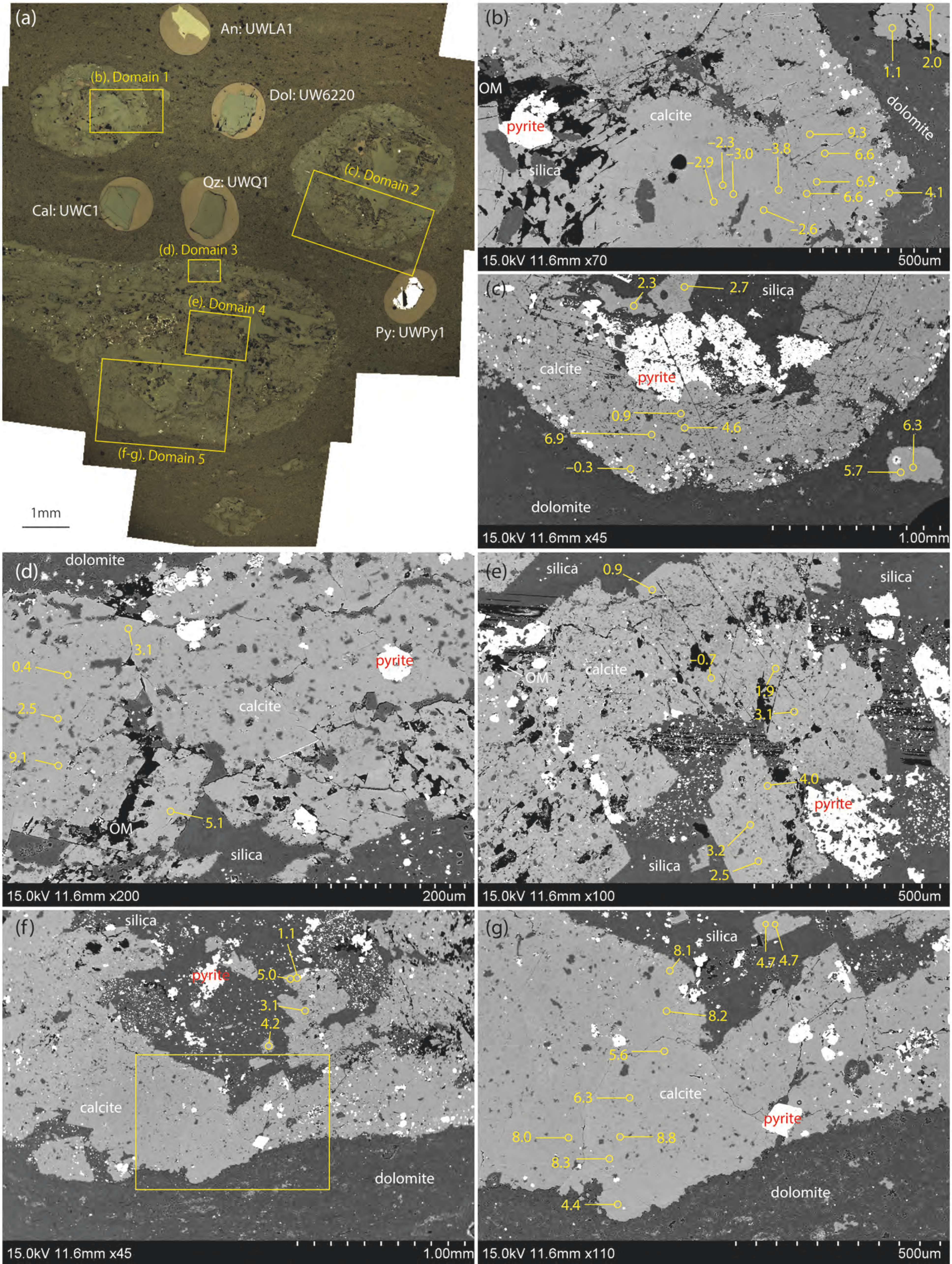
(a)
An: UWLA1
(b). Domain 1
Dol: UW6220
(c). Domain 2
Qz: UWQ1
Cal: UWC1
(d). Domain 3
(e). Domain 4
Py: UWPy1
(f-g). Domain 5
1mm
(b)
OM
pyrite
calcite
silica
dolomite
1.1
2.0
9.3
6.6
6.9
6.6
4.1
−2.3
−3.0
−3.8
−2.9
−2.6
15.0kV 11.6mm x70
500um
(c)
2.3
2.7
silica
calcite
pyrite
0.9
4.6
6.9
−0.3
6.3
5.7
dolomite
15.0kV 11.6mm x45
1.00mm
(d)
dolomite
3.1
0.4
2.5
9.1
pyrite
calcite
OM
5.1
silica
15.0kV 11.6mm x200
200um
(e)
silica
0.9
silica
−0.7
OM
calcite
1.9
3.1
4.0
pyrite
3.2
2.5
silica
15.0kV 11.6mm x100
500um
(f)
silica
1.1
pyrite
5.0
3.1
4.2
calcite
dolomite
15.0kV 11.6mm x45
1.00mm
(g)
8.1
silica
4.7
4.7
8.2
5.6
6.3
calcite
pyrite
8.0
8.8
8.3
4.4
dolomite
15.0kV 11.6mm x110
500um

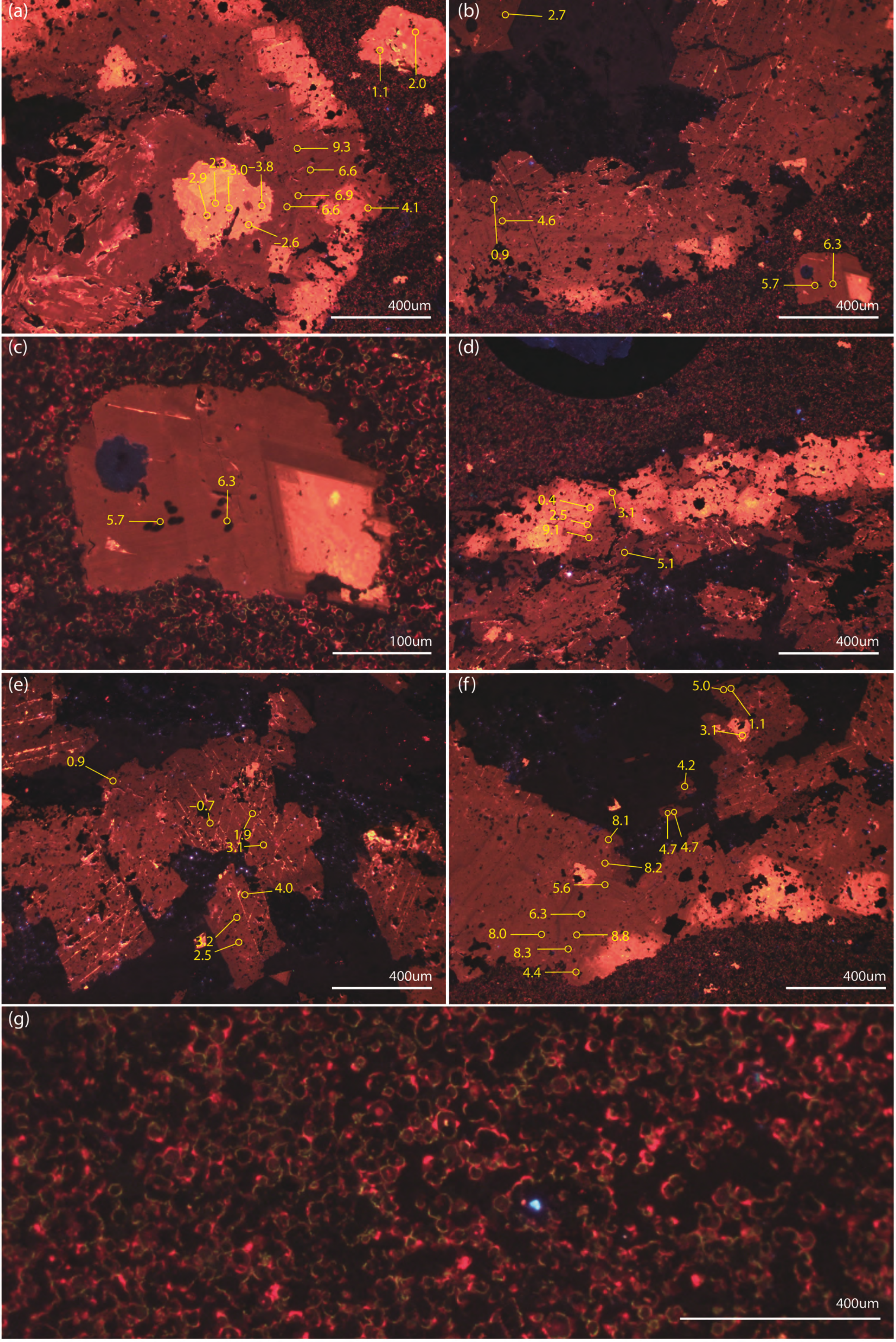
(a)
1.1
2.0
9.3
6.6
−2.3
3.0
−3.8
−2.9
6.9
6.6
4.1
−2.6
400um
(b)
2.7
4.6
0.9
6.3
5.7
400um
(c)
6.3
5.7
100um
(d)
0.4
3.1
2.5
9.1
5.1
400um
(e)
0.9
−0.7
1.9
3.1
4.0
3.2
2.5
400um
(f)
5.0
1.1
3.1
4.2
8.1
4.7
4.7
8.2
5.6
6.3
8.0
8.8
8.3
4.4
400um
(g)
400um

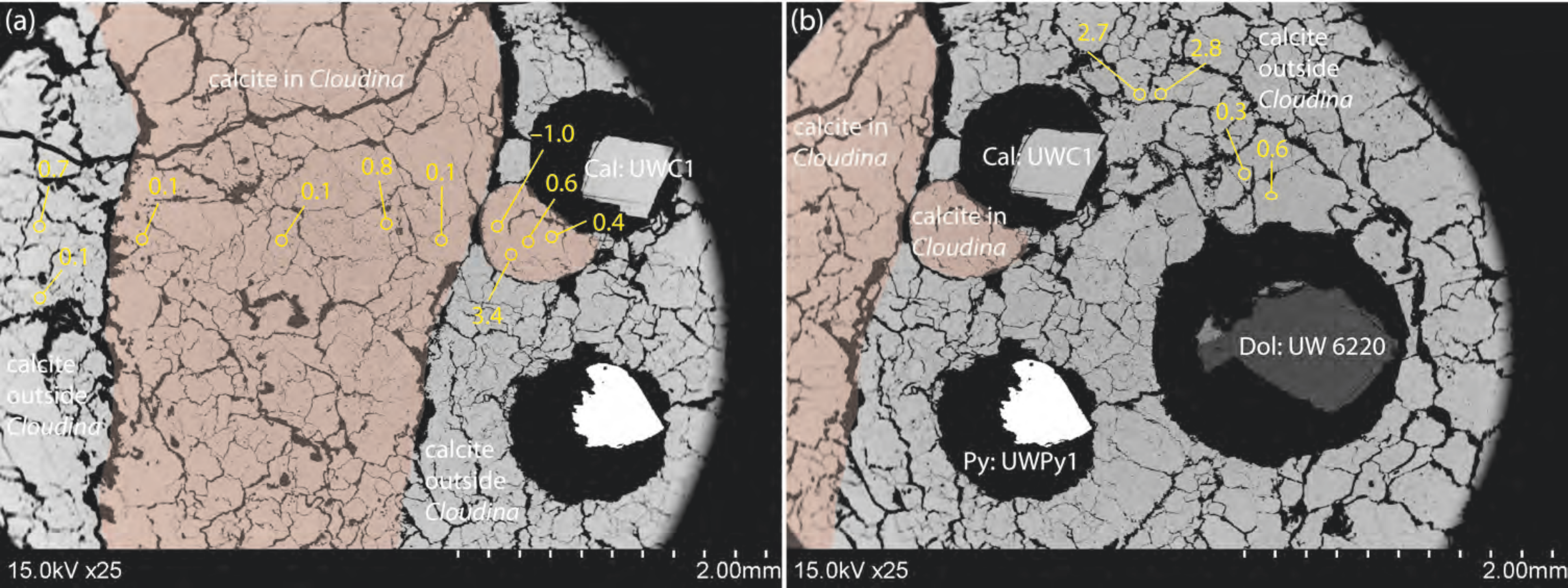
(a)
calcite in *Cloudina*
−1.0
0.7
0.1
0.1
0.8
0.1
Cal: UWC1
0.6
0.4
0.1
3.4
calcite outside *Cloudina*
calcite outside *Cloudina*
15.0kV x25
2.00mm
(b)
2.7
2.8
calcite outside *Cloudina*
calcite in *Cloudina*
0.3
0.6
Cal: UWC1
calcite in *Cloudina*
Dol: UW 6220
Py: UWPy1
15.0kV x25
2.00mm

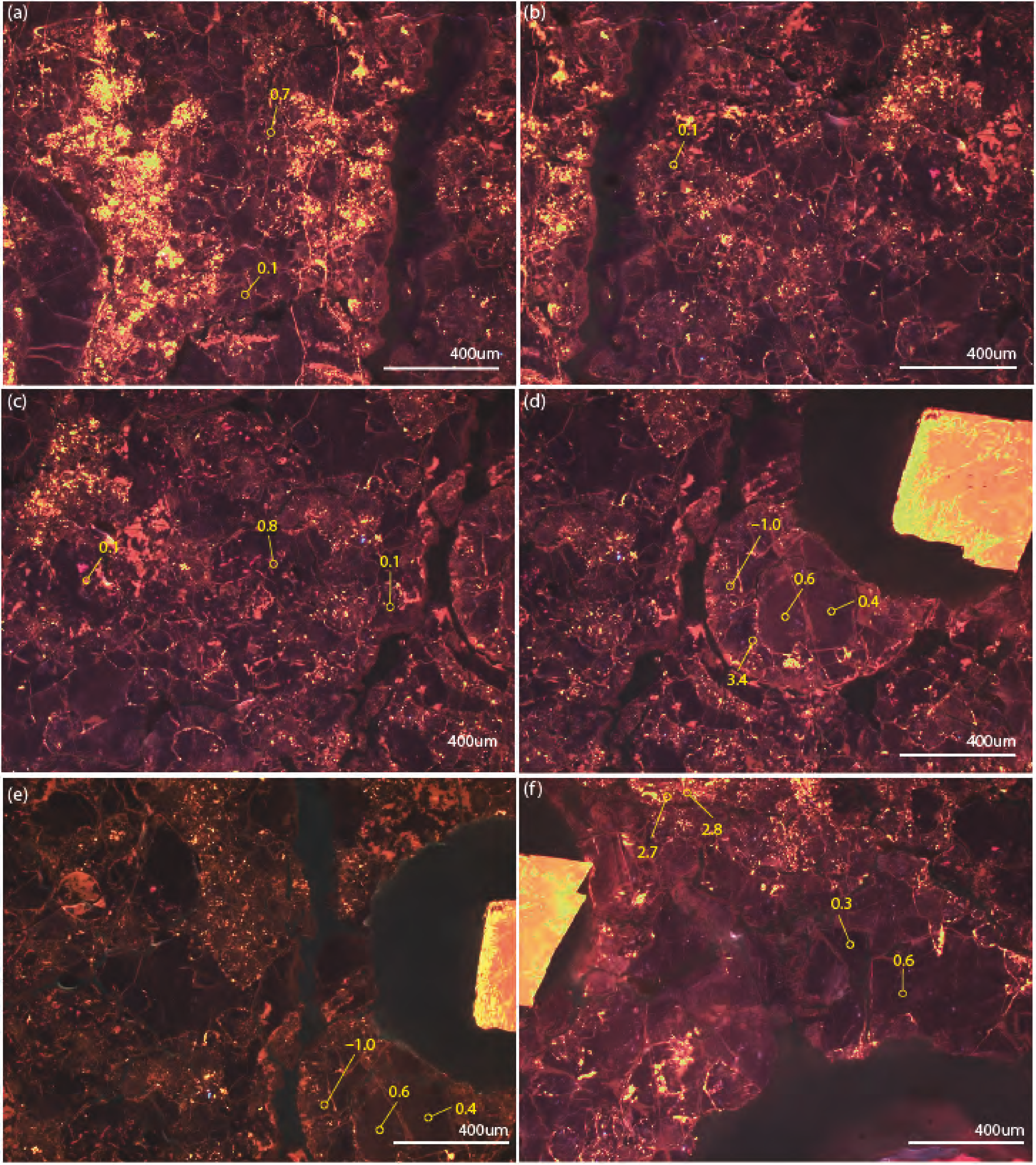
(a)
0.7
0.1
400um
(b)
0.1
400um
(c)
0.1
0.8
0.1
400um
(d)
−1.0
0.6
0.4
3.4
400um
(e)
−1.0
0.6
0.4
400um
(f)
2.7
2.8
0.3
0.6
400um

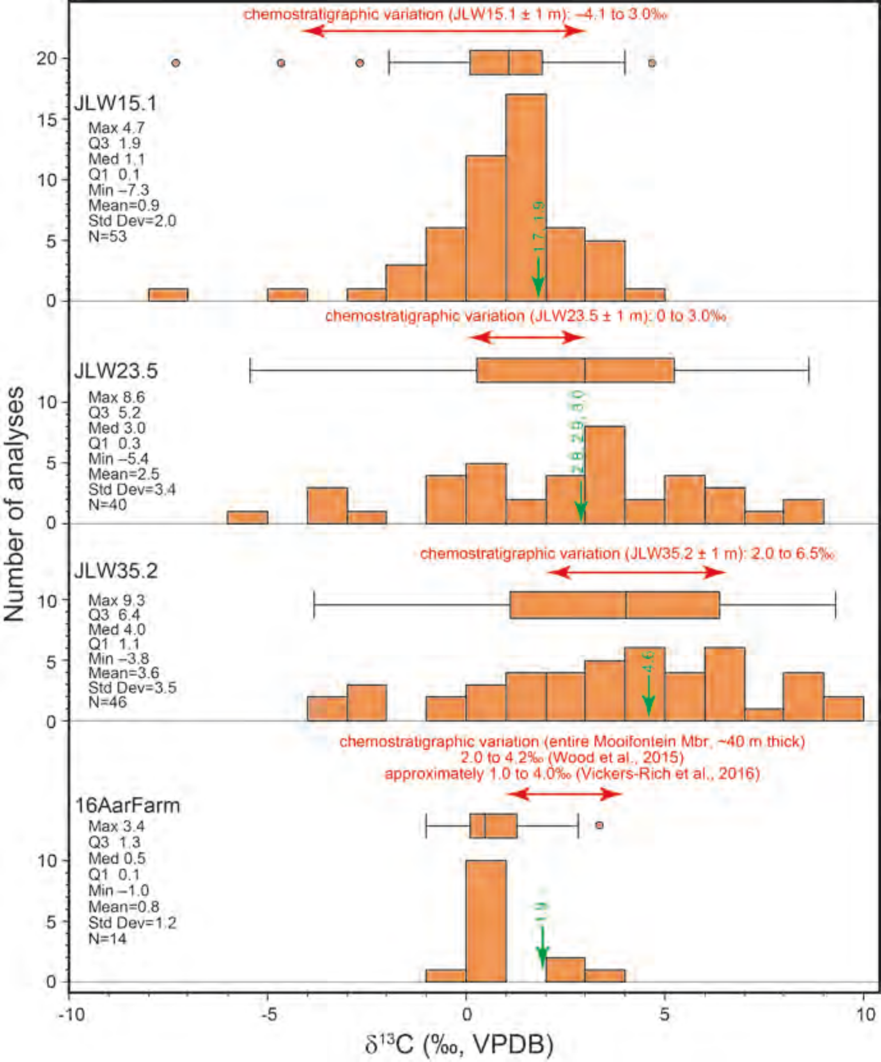

chemostratigraphic variation (JLW15.1 ± 1 m): −4.1 to 3.0‰
JLW15.1
Max 4.7
Q3 1.9
Med 1.1
Q1 0.1
Min −7.3
Mean=0.9
Std Dev=2.0
N=53
17, 19
chemostratigraphic variation (JLW23.5 ± 1 m): 0 to 3.0‰
JLW23.5
Max 8.6
Q3 5.2
Med 3.0
Q1 0.3
Min −5.4
Mean=2.5
Std Dev=3.4
N=40
28, 29, 30
chemostratigraphic variation (JLW35.2 ± 1 m): 2.0 to 6.5‰
JLW35.2
Max 9.3
Q3 6.4
Med 4.0
Q1 1.1
Min −3.8
Mean=3.6
Std Dev=3.5
N=46
4.6
chemostratigraphic variation (entire Mooifontein Mbr, ~40 m thick)
2.0 to 4.2‰ (Wood et al., 2015)
approximately 1.0 to 4.0‰ (Vickers-Rich et al., 2016)
16AarFarm
Max 3.4
Q3 1.3
Med 0.5
Q1 0.1
Min −1.0
Mean=0.8
Std Dev=1.2
N=14
Number of analyses
20
15
10
5
0
-10
-5
0
5
10
δ13C (‰, VPDB)

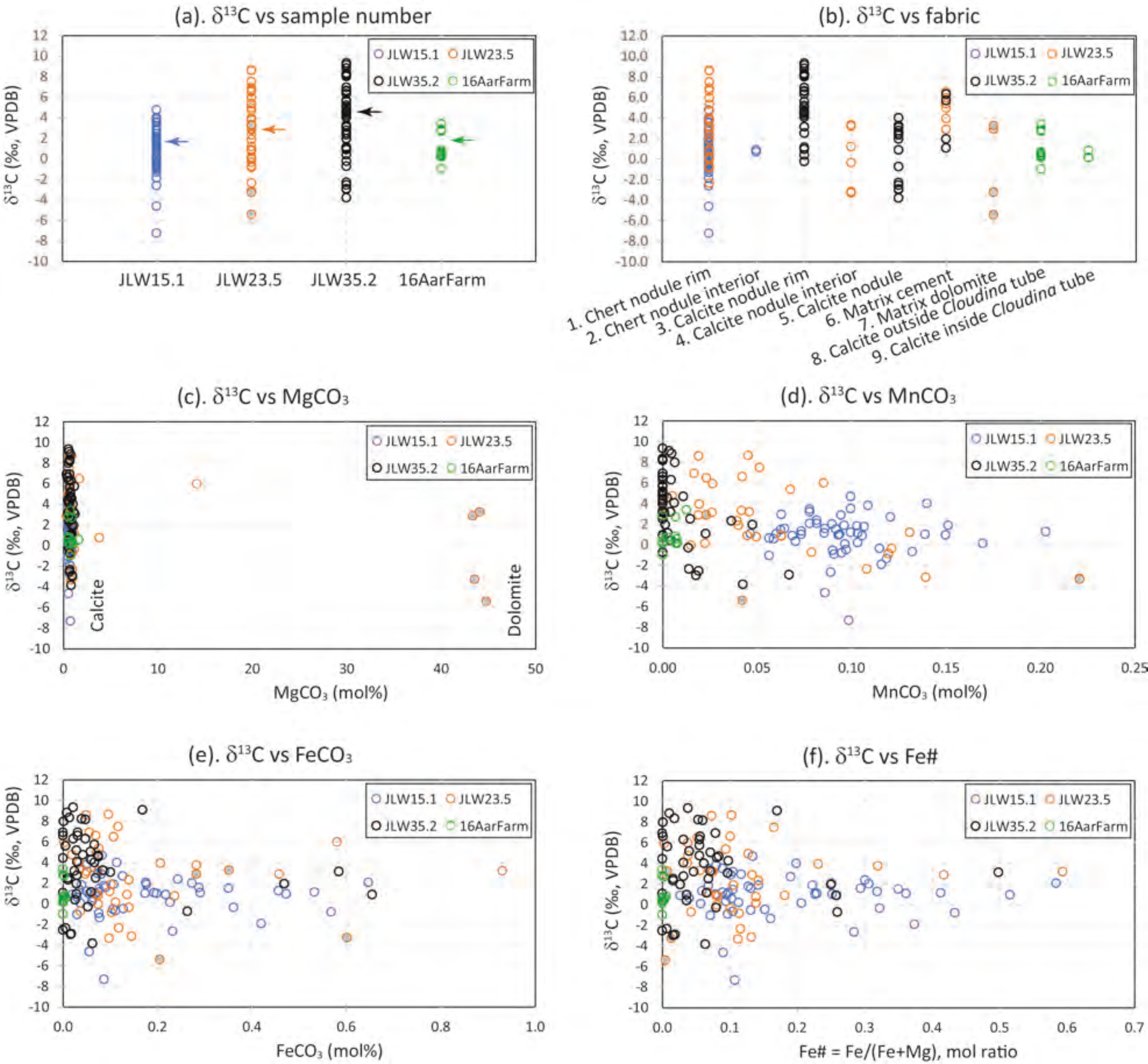
(a). δ13C vs sample number
δ13C (‰, VPDB)
JLW15.1
JLW23.5
JLW35.2
16AarFarm
12
10
8
6
4
2
0
-2
-4
-6
-8
-10
(b). δ13C vs fabric
δ13C (‰, VPDB)
12.0
10.0
8.0
6.0
4.0
2.0
0.0
-2.0
-4.0
-6.0
-8.0
-10.0
JLW15.1
JLW23.5
JLW35.2
16AarFarm
1. Chert nodule rim
2. Chert nodule interior
3. Calcite nodule rim
4. Calcite nodule interior
5. Calcite nodule
6. Matrix cement
7. Matrix dolomite
8. Calcite outside Cloudina tube
9. Calcite inside Cloudina tube
(c). δ13C vs MgCO3
δ13C (‰, VPDB)
MgCO3 (mol%)
0
10
20
30
40
50
Calcite
Dolomite
JLW15.1
JLW23.5
JLW35.2
16AarFarm
(d). δ13C vs MnCO3
δ13C (‰, VPDB)
MnCO3 (mol%)
0.00
0.05
0.10
0.15
0.20
0.25
JLW15.1
JLW23.5
JLW35.2
16AarFarm
(e). δ13C vs FeCO3
δ13C (‰, VPDB)
FeCO3 (mol%)
0.0
0.2
0.4
0.6
0.8
1.0
JLW15.1
JLW23.5
JLW35.2
16AarFarm
(f). δ13C vs Fe#
δ13C (‰, VPDB)
Fe# = Fe/(Fe+Mg), mol ratio
0.0
0.1
0.2
0.3
0.4
0.5
0.6
0.7
JLW15.1
JLW23.5
JLW35.2
16AarFarm